

HUBBLE/COS OBSERVATIONS OF THE QUASAR HE 2347–4342: PROBING THE EPOCH OF He II PATCHY REIONIZATION AT REDSHIFTS $Z = 2.4 - 2.9$

J. MICHAEL SHULL, KEVIN FRANCE, CHARLES W. DANFORTH, BRITTON SMITH

CASA, Department of Astrophysical and Planetary Sciences, University of Colorado, 389-UCB, Boulder, CO 80309;
 michael.shull@colorado.edu, kevin.france@colorado.edu, charles.danforth@colorado.edu, britton.smith@colorado.edu

AND JASON TUMLINSON

Space Telescope Science Institute, Baltimore, MD 21218; tumlinson@stsci.edu

Accepted for publication in The Astrophysical Journal

ABSTRACT

We report ultraviolet spectra of the high-redshift ($z_{\text{em}} \approx 2.9$) quasar, HE 2347–4342, taken by the Cosmic Origins Spectrograph (COS) on the *Hubble Space Telescope* (HST). Spectra in the G130M (medium-resolution, 1135–1440 Å) and G140L (low-resolution, 1030–2000 Å) gratings exhibit patchy Gunn-Peterson absorption in the 303.78 Å Ly α line of He II between $z = 2.39$ – 2.87 (G140L) and $z = 2.74$ – 2.90 (G130M). With COS, we obtain better spectral resolution, higher-S/N, and better determined backgrounds than previous studies, with sensitivity to abundance fractions $x_{\text{HeII}} \approx 0.01$ in filaments of the cosmic web. The He II optical depths from COS are higher than those with the *Far Ultraviolet Spectroscopic Explorer* (FUSE) and range from $\tau_{\text{HeII}} \leq 0.02$ to $\tau_{\text{HeII}} \geq 5$, with a slow recovery in mean optical depth to $\langle \tau_{\text{HeII}} \rangle \leq 2$ at $z < 2.7$. The He II/H I optical-depth ratio varies ($\eta \approx 10$ – 100 for $2.4 < z < 2.73$, and $\eta = 5$ – 500 for $2.75 < z < 2.89$) on scales $\Delta z \lesssim 0.01$ (10.8 Mpc in comoving radial distance at $z = 2.8$), with numerous flux-transmission windows between 1135–1186 Å. The He II absorption extends to 1186.26 Å ($z = 2.905$), including associated absorbers with $z_{\text{abs}} \approx z_{\text{QSO}}$ and minimal “proximity effect” of flux transmission at the He II edge. We propose a QSO systemic redshift $z_{\text{QSO}} = 2.904 \pm 0.002$, some $\Delta z = 0.019$ higher than that derived from O I $\lambda 1302$ emission. Three long troughs (4–10 Å or 25–60 Mpc comoving distance) of strong He II absorption between $z = 2.75$ – 2.90 are uncharacteristic of the intergalactic medium if He II reionized at $z_r \approx 3$. Contrary to recent indirect estimates ($z_r = 3.2 \pm 0.2$) from H I optical depths, the epoch of He II reionization may extend to $z \lesssim 2.7$.

Subject headings: quasars: reionization — individual: HE 2347-4342 galaxies: active, intergalactic medium, quasars: absorption lines, ultraviolet: general

1. INTRODUCTION

The epoch of reionization in hydrogen has become a topic of considerable interest (Barkana & Loeb 2001; Fan, Carilli, & Keating 2006; Meiksin 2009; Furlanetto et al. 2009) as a probe of the transition from neutral to ionized hydrogen in the intergalactic medium (IGM). This transition occurred somewhere between redshifts $z = 6$ – 12 , marking the exit from the cosmic “dark ages”, beginning at the time when the first stars and galaxies formed at redshifts $z > 30$ (Tegmark et al. 1997; Ricotti, Gnedin, & Shull 2002; Trenti & Shull 2010). Helium underwent similar reionization from He II to He III (that is, from He⁺ to He²⁺) at $z = 2.8 \pm 0.2$ (Reimers et al. 1997; Shull et al. 2004), most likely mediated by the harder ($E \geq 54.4$ eV) radiation from quasars and other active galactic nuclei (AGN). With a 4 ryd ionization potential, He⁺ is harder to ionize than H⁰, and He²⁺ recombines 5–6 times faster than H⁺ (Osterbrock & Ferland 2006; Fardal, Giroux, & Shull 1998). For these reasons, and the fact that most hot stars lack strong 4 ryd continua, it is believed that AGN are the primary agents of He II reionization. Ionization models find that, owing to its resilience, He⁺ is much more abundant than H⁰, with predicted column-density ratios $\eta \equiv N(\text{He II})/N(\text{H I}) \approx$

50–100 (Miralda-Escudé et al. 1996; Fardal, Giroux, & Shull 1998).

Determining when and how the universe was ionized has been an important question in cosmology for decades (Gunn & Peterson 1965; Sunyaev 1977). Although recent progress has led to quantitative constraints, we still do not know whether galaxies are the sole agents of hydrogen reionization, and the epoch of reionization remains uncertain. We *do* know that hydrogen reionization in the IGM is complete by $z \approx 6$, based on the rapid evolution between redshifts $z = 6.2$ and $z \approx 5$ of Ly α Gunn-Peterson (GP) absorption from neutral hydrogen along lines of sight to QSOs (Fan et al. 2002; Gnedin 2004). The optical depth of the cosmic microwave background (Komatsu et al. 2010) sets a 3σ constraint on instantaneous reionization at $z_r > 6.5$ and a 1σ confidence interval of $z_r = 10.5 \pm 1.2$. A limit $z_r \geq 7$ is set by the detection of Ly α emitters at $z = 6.5$ (major evolution in the observed luminosity function would be expected if neutral gas were present around the emitters). These observations are in line with Λ CDM simulations (Trac & Cen 2007; Cen 2003; Gnedin 2004) and ionization-front (I-front) models (Venkatesan, Tumlinson & Shull 2003; Bolton & Haehnelt 2007; Shull & Venkatesan 2008). The current data leave open several hydrogen ionization sce-

narios, some involving simple reionization at $z_r \approx 10$ and others with more complex ionization histories that depend on the star-formation rate at $z = 7 - 20$ and the transition from Pop III to Pop II stars. Numerical models of the reionization process often follow the expansion and overlap of I-fronts, but the details are complicated by geometric uncertainties in the ionizing sources, higher recombination rates in denser gas, and radiative transfer of Lyman continuum (LyC) photons. In particular, the gas is highly structured in both density and temperature.

The He II reionization epoch (z_r) and ionization processes are also poorly characterized. The thermal evolution of the IGM includes many subtle effects, with degeneracies arising from fluctuations in density, temperature, and ionization fraction, as well as spectral hardness of the ionizing sources. Previous estimates of $z_r \approx 3$ were based on indirect measurements of temperature, ionization, and average optical depth of Ly α lines of H I, and on apparent shifts in Si IV/C IV absorption-line ratios arising from changes in the 4-ryd continuum radiation field as He II was ionized to He III. Early estimates of the IGM temperature evolution and equation of state from H I line widths suggested a change at $z \approx 3$ (Ricotti, Gnedin, & Shull 2000; Schaye et al. 2000). Theuns et al. (2002) analyzed the average optical depth of (H I) Ly α lines in 1061 quasar spectra, using low-resolution data from the Sloan Digital Sky Survey (Bernardi et al. 2003). From a weak dip in $\tau_{\text{eff}}(z)$ at $z \approx 3.1$, these authors suggested that He II reionization started at redshift $z \approx 3.4$ and lasted until $z \approx 3.0$. Several recent studies with higher-resolution spectroscopic data have not confirmed the τ_{eff} feature (McDonald et al. 2005; Kim et al. 2007). Faucher-Giguere et al. (2008) found a feature in $\tau_{\text{eff}}(\text{H I})$ near $z = 3.2$, in a sample of 86 high-resolution, high-S/N quasar spectra taken with Keck (ESI, HIRES) and Magellan (MIKE). However, they question the reionization explanation of the depth and narrow redshift extent. They also note that at least three physical effects could produce a feature in $\tau_{\text{eff}}(z)$: changes in IGM temperature, electron number density, and ionizing background. Recent numerical simulations (Bolton et al. 2009; McQuinn et al. 2009; Lidz et al. 2010) also question whether He II reionization is responsible for the proposed feature in $\tau_{\text{eff}}(z)$ at $z \approx 3.2 \pm 0.2$.

The most direct estimates of He II reionization come from far-ultraviolet spectra of He II Lyman- α absorption toward high-redshift AGN. Because of strong Galactic interstellar absorption in the H I Lyman continuum, the He II $\lambda 304$ line is only observable in the far ultraviolet, at redshifts $z \geq 2$ when the line shifts longward of 912 Å. A small number of bright AGN at $z = 2.9 - 3.3$ have been observed with the *Hubble Space Telescope* (*HST*) and the *Far Ultraviolet Spectroscopic Explorer* (*FUSE*). These data show moderate optical depths in the He II line, ranging up to $\tau_{\text{HeII}} = 3 - 4$, with a gradual recovery of transmission ($\tau_{\text{HeII}} < 1$) at $z < 2.7$. The best He II absorption data have been acquired toward three high-redshift AGN: Q0302-003 (Jakobsen et al. 1994; Hogan, Anderson, & Rugers 1997; Heap et al. 2000); and HE 2347-4342 (Reimers et al. 1997; Kriss et al. 2001; Smette et al. 2002; Shull et al. 2004; Zheng et al. 2004); and HS 1700+6416 (Davidsen, Kriss, & Zheng 1996; Fechner et al. 2006). From an analysis of

the He II optical-depth evolution in moderate-resolution *FUSE* data toward HE 2347-4342, Shull et al. (2004) suggested that the reionization epoch of He⁺ occurred at $z_r = 2.8 \pm 0.2$.

Observations of He II with *HST* and *FUSE* also constrain the thermodynamic state of the IGM and the spectra of ionizing sources. For example, the high abundance ratio, $N(\text{He II})/N(\text{H I}) \approx 50 - 100$, observed toward HE 2347-4342 and HS 1700+6416 (Kriss et al. 2001; Smette et al. 2002; Shull et al. 2004; Zheng et al. 2004; Fechner et al. 2006) requires a soft ionizing radiation field, $F_\nu \propto \nu^{-\alpha_s}$, with mean spectral index $\langle \alpha_s \rangle \approx 1.8$ (Fardal et al. 1998). As observed in the QSO rest-frame, the EUV (1-2 ryd) spectral indices of quasars exhibit a wide range (Telfer et al. 2002; Scott et al. 2004). More intriguing are the spectroscopic observations of He II and H I taken by *FUSE*, the Keck Telescope, and the Very Large Telescope (VLT). Kriss et al. (2001) and Shull et al. (2004) report variations in $\eta = 20 - 200$ over 2-10 Mpc scales ($\Delta z \approx 0.002 - 0.01$) which imply spatial fluctuations in the radiation field at the ionization edges of H I (1 ryd) and He II (4 ryd). Most of these variations probably arise in the 4 ryd continuum, whose photons have greater penetrating power. These flux differences at 1 ryd and 4 ryd are then amplified by absorption and reprocessing by the IGM (Haardt & Madau 1996; Fardal et al. 1998).

In this paper, we present new, high-quality, far-UV spectroscopic observations of intergalactic He II absorption toward HE 2347-4342, using the Cosmic Origins Spectrograph (COS) on *HST* (Green et al. 2010; Osterman et al. 2010). This target is of considerable interest as a bright ($V = 16.1$, $z \approx 2.9$) continuum source, previously observed by the *FUSE*, Keck, and VLT spectrographs to study intergalactic Ly α absorption in both H I and He II. HE 2347-4342 is the first of three AGN targets scheduled for COS guaranteed-time observations of the He II reionization epoch. The data were acquired with both the moderate-resolution G130M grating ($R \approx 18,000$, $\lambda = 1135 - 1440$ Å) and the low-resolution G140L grating ($R \approx 1500$, $\lambda = 1030 - 2000$ Å). In the 303.78 Å line of He II, these wavelength bands allow us to probe redshifts down to $z_{\text{HeII}} = 2.735$ (G130M) and $z_{\text{HeII}} \approx 2.39$ (G140L). The COS data enable many improvements compared to previous studies. First, the high far-UV throughput of the COS/G130M grating provides higher signal-to-noise (S/N) and better photometric accuracy. Second, the low background of the COS detectors allows us to detect very weak flux-transmission through the IGM, characterize low flux levels in He II absorption troughs, and probe regions of high optical depth, $\tau_{\text{HeII}} \gtrsim 5$. Finally, low-resolution G140L spectra (1000-2000 Å) allow us to study the recovery of the He II optical depth at $z < 2.7$ and characterize the continuum longward of the He II edge.

In §2 we discuss the observations and data reduction techniques for both G130M and G140L gratings. In §3 we display the fitted quasar continuum, $F_\lambda \propto \lambda^{-3.0 \pm 0.1}$, which we use to extrapolate below the He II edge at 1186.2 Å. From this continuum and the transmitted fluxes, we derive He II optical depths in the Ly α forest and analyze the fluctuating absorption. We observe minimal effects of local photoionization expected from prox-

imity to this very luminous QSO. In the He II Ly α forest at $2.4 < z < 2.9$, we see narrow (2–5 Å, 12–30 Mpc of comoving radial distance) windows of partial flux transmission, which we interpret as “patchy He II reionization”, interspersed with broad He II absorption troughs (4–10 Å intervals, 25–60 Mpc) with high optical depths, $\tau_{\text{HeII}} \geq 5$. At $\lambda < 1130$ Å ($z_{\text{HeII}} < 2.72$) the mean opacity drops to $\langle \tau_{\text{HeII}} \rangle \lesssim 2$, consistent with the overlap of the He II I-fronts. Because He II is much more abundant than H I, its opacity through the cosmic web remains high.

In §4 we summarize our observations and their implications for the He II reionization epoch. With reasonable assumptions about the physical state of the IGM at $z = 2 - 3$, borne out by studies of H I and He II Ly α -forest absorption and cosmological simulations, we can probe the He II reionization epoch down to fractional ionization $x_{\text{HeII}} \geq (0.01)(0.1/\delta_H)(\tau_{\text{HeII}}/5)$ in underdense regions ($\delta_H = 0.1 - 1$) relative to the mean baryon density of the cosmic web. This ionization level provides much greater sensitivity to conditions at $z \approx 2.8$ than possible with H I at $z \approx 6$ (Fan et al. 2006). Coupled with galaxy surveys, cosmological simulations, and photoionization modeling, these UV spectra will help us understand the propagation and overlap of the helium ionization fronts.

2. HST-COS OBSERVATIONS AND DATA REDUCTION

2.1. Wavelength Scale and Fluxes

HE 2347–4342 was observed with the short-wavelength, medium-resolution far-UV mode of HST-COS (G130M) on 2009 November 05 for a total of 28,459 s. Descriptions of the COS instrument and on-orbit performance characteristics are in preparation (Green et al. 2010; Osterman et al. 2010). In order to achieve continuous spectral coverage across the G130M bandpass ($1135 \text{ Å} \lesssim \lambda \lesssim 1440 \text{ Å}$) and to minimize fixed-pattern noise, we made observations at two central wavelength settings (1291 Å and 1300 Å) with four focal-plane offset locations in each grating setting (FP-POS = 1, 2, 3, 4). This combination of grating settings ensures the highest signal-to-noise observations at the shortest wavelengths available to the G130M mode ($z_{\text{HeII}} \approx 2.73 - 3.00$) at a resolving power of $R \equiv (\lambda/\Delta\lambda) \approx 18,000$ ($\Delta v_{\text{FWHM}} \approx 17 \text{ km s}^{-1}$).

In addition, COS observed HE 2347–4342 in the low-resolution G140L mode for 11,558 s on 2009 November 06. The G140L Segment-A data provide some overlap with the G130M observations between 1240–1440 Å, and they extend our low-resolution spectral coverage ($R \approx 1500$) out to $\lambda \approx 2000$ Å. From G140L segment-B observations and custom data-processing steps described in Section 2.2, we extend our reliable spectral coverage over part of the G140L bandpass, between 1030–1175 Å. Table 1 lists the relevant COS observational parameters for the data sets used in this work.

All observations were centered on the QSO target, HE 2347–4342 at J2000 coordinates (R.A. = $23^{\text{h}}50^{\text{m}}34.23^{\text{s}}$, Decl. = $-43^{\circ}25'59.80''$). COS performed NUV imaging target acquisitions with the MIR-RORA/PSA mode, yielding good centering in the COS aperture to maximize throughput and resolving power.

TABLE 1
HE 2347–4342 OBSERVING LOG

Date	COS Mode	λ_c (Å)	FP-POS	Exp	T_{exp} (s)
2009 Nov 05	G130M	1291 Å	1,2,3,4	9	16535
2009 Nov 05	G130M	1300 Å	1,2,3,4	9	11924
2009 Nov 06	G140L	1230 Å	1,2,3,4	4	11558

The G130M data were processed with the COS calibration pipeline, CALCOS¹ v2.11b, and combined with a custom IDL coaddition procedure. The analog nature of the COS micro-channel plate makes it susceptible to temperature changes. Electronically injected pulses (stims) at opposite corners of the detector allow for the tracking and correction of any drift (wavelength zero-point) and/or stretch (dispersion solution) of the recorded data location as a function of temperature. At the beginning of the observations of HE 2347–4342, the detector proved to be substantially colder than the nominal operating temperature of the micro-channel plate. This allowed one of the electronic stim-pulses to accumulate at the bottom of the detector, compromising the wavelength solution for the first four G130M exposures. The detector warmed to the normal operating range for the remaining G130M observations. We reprocessed the earlier exposures using extrapolated stim positions to ensure a consistent wavelength solution over the course of the observations. The G140L data were unaffected.

Flat-fielding, alignment, and coaddition of the processed COS/G130M exposures were carried out using IDL routines developed by the COS GTO team specifically for COS FUV data². First, the data were corrected for fixed-pattern instrumental features. Although attempts at a true “flat-fielding” of COS data show promise, the technique is not yet sufficiently robust to improve data of moderate S/N. The quantum efficiency is improved by the presence of a series of wires, called the quantum-efficiency grid, placed above the detector. These wires create shadows in the spectrum that are removed during data reduction. An ion-repellor grid reduces the background rate by preventing low-energy thermal ions from entering the open-faced detector. We are able to correct the narrow shadows of $\sim 15\%$ opacity arising from the grid wires. A one-dimensional map of grid-wire opacity for each detector was shifted from detector coordinates into wavelength space and divided from the flux and error vectors. Exposure time in the location of grid wires was decreased by ~ 0.7 , giving these pixels less weight in the final coaddition. We also modified the error vector and local exposure time at the edges of the detector segments to underweight the flux contributions from these regions. With a total of eight different wavelength settings in the final co-addition, any residual instrumental artifacts from grid-wire shadows and detector segment boundaries should have little effect on the final spectrum.

¹ See the *HST* Cycle 18 COS Instrument Handbook for more details:

http://www.stsci.edu/hst/cos/documents/handbooks/current/cos_cover.html

² See <http://casa.colorado.edu/~danforth/costools.html> for our coaddition and flat-fielding algorithm and additional discussion.

We performed two sets of wavelength-scale shifts. First, the G130M exposures were aligned with each other and interpolated onto a common wavelength scale. Then, we transferred the G130M wavelengths to a ground-based reference frame of the H I data, taken by D. Reimers with the VLT/UVES (Ultraviolet Visual Echelle Spectrograph) in ESO program 071.A-0066. These data were used in the He II analysis paper of *FUSE* data (Shull et al. (2004)). One exposure in each COS detector was picked as a wavelength reference, and the remaining exposures were cross-correlated with it. The wavelength region of cross-correlation for each case was picked to include a strong interstellar absorption feature, although shifts were typically a resolution element or less. Residual errors on the target centering within the COS aperture caused a systematic shift between the strong interstellar lines and their expected LSR velocities. The COS wavelength solution is relatively accurate, but it may suffer from linear offsets from an absolute frame. Since our later analysis involves comparing the rapidly-varying H I (optical) and He II (UV) profiles, wavelength alignment is critical. The only absorption features in the normalized VLT data clearly not associated with the Ly α forest are a pair of narrow absorbers at 4787.12 Å and 4795.08 Å, consistent in relative strength and separation with the C IV doublet at 1548.195 and 1550.770 Å, redshifted to $z = 2.0921$. At this redshift, COS/G130M covers 384–466 Å. The C III λ 386.20 line at 1194.1 Å in the COS data corresponds to the C IV doublet in the optical data, with similar line profiles. We therefore shift the COS data by +0.07 Å (approximately one G130M resolution element) to align with the optical spectra.

The flux at each position was taken to be the exposure-time weighted mean of flux. Since exposure time was reduced in certain wavelength locations, as noted above, pixels near detector edges and where grid-wire shadows were removed received less weight than those in less suspect locations. The combined G130M data show $S/N \sim 25$ per 7-pixel resolution element, sufficient to detect narrow absorption features near 1200 Å down to equivalent widths $W_\lambda \gtrsim 10$ mÅ at 4σ significance. The G140L observations were originally processed with CALCOS 2.11b. However, the $\lambda < 1200$ Å data from this processing is not appropriate for scientific analysis. We describe our custom processing in Section 2.2.

Figure 1 shows the G130M/G140L continuum from 1200 Å to 2000 Å, which we have fitted and extrapolated below the He II edge at 1186.2 Å. The G140L wavelengths were shifted to match G130M, with no corrections needed to match G130M and G140L fluxes. These curves were de-reddened using color excess, $E(B - V) = 0.022$, corresponding to column density $\log N_{\text{HI}} = 20.06$ derived by fitting interstellar Ly α absorption. We adopted a standard interstellar ratio, $N_{\text{HI}} = (5.3 \times 10^{21} \text{ cm}^{-2} \text{ mag}^{-1})E(B - V)$, from Shull & Van Steenberg (1985) and Diplis & Savage (1994) and used the UV selective extinction curve of Fitzpatrick & Massa (1999). Our derived extinction, $E(B - V) = 0.022$, lies intermediate between previous values of $E(B - V) = 0.0387$ (Reimers et al. 1997) and $E(B - V) = 0.014$ (Smette et al. 2002). Figure 2 shows the G130M spectrum ($\lambda < 1208$ Å) with prominent He II absorption troughs,

TABLE 2
HE 2347-4342 SIGHT LINE HE II ABSORPTION^a

z_c	Δz	λ_c (Å)	τ_{HeII}	COS Mode	Notes ^b
2.90151	0.00400	1185.20	≥ 5	G130M	...
2.89765	0.00800	1184.03	≥ 5	G130M	...
2.88721	0.00823	1180.86	≥ 5	G130M	...
2.87445	0.01317	1176.98	≥ 5	G130M	Z04-3A
2.84700	0.03456	1168.64	≥ 5	G130M	Z04-3CDE
2.77471	0.05267	1146.68	≥ 5	G130M	Z04-3HIJ
2.71324	0.00823	1128.01	3.3 ± 0.25	G140L	...
2.69082	0.01646	1121.20	3.0 ± 0.50	G140L	...
2.66414	0.00494	1113.09	1.8 ± 0.25	G140L	...
2.65061	0.00494	1108.98	1.5 ± 0.25	G140L	...
2.63785	0.01317	1105.11	2.3 ± 0.25	G140L	...
2.61814	0.00988	1099.12	1.3 ± 0.50	G140L	...
2.59804	0.00988	1093.01	2.0 ± 1.0	G140L	...
2.57059	0.01317	1084.67	3.5 ± 1.0	G140L	...
2.55000	0.02008	1078.42	1.0 ± 0.25	G140L	...
2.52999	0.02008	1072.34	2.5 ± 0.50	G140L	...
2.49327	0.01975	1061.19	2.8 ± 1.0	G140L	...
2.47001	0.02008	1054.12	1.5 ± 0.50	G140L	...
2.43683	0.01811	1044.04	1.7 ± 0.50	G140L	...

^a Average He II optical depth τ_{HeII} was computed from flux transmission averaged over redshift bins $z_c \pm \Delta z$ at centroid wavelengths λ_c . Errors in τ_{HeII} are conservatively rounded to nearest 0.25.

^b These three He II complexes noted Z04-3*n* were identified in Table 3 of Zheng et al. (2004).

numerous flux-transmission windows shortward of the He II edge, and the two proposed QSO systemic redshifts, $z_{\text{QSO}} = 2.885 \pm 0.005$ (Reimers et al. 1997) and $z_{\text{QSO}} = 2.904 \pm 0.002$ (this paper). This issue is discussed further in Section 3.1.

The strong He II features are listed in Table 2, with the He II optical depths calculated from the depth of flux transmission, $\tau_{\text{HeII}} = \ln(F_0/F_\lambda)$, relative to the extrapolated continuum F_0 . Uncertainties in τ_{HeII} were computed as root-mean-square averages over redshift bins, Δz , ranging from 0.004 to 0.02 at wavelength centroids λ_c . We conservatively rounded errors to the nearest 0.25 in τ_{HeII} , using uncertainties arising from converting errors in flux transmission to errors in optical depth. In regions of lower S/N in the G140L grating ($z \lesssim 2.6$), we smoothed over two resolution elements (~ 2 Å) to reduce the noise before the optical depth and error were evaluated. The G140L-B spectra shown in Figure 1 were smoothed over three resolution elements.

2.2. Data Processing: COS G140L Segment B

During the Servicing Mission-4 Observatory Verification (SMOV-4) period, it was discovered that the MgF₂/Al mirrors of *HST* have retained approximately 80% of their pre-flight reflectivity at $\lambda < 1175$ Å (McCandliss et al. 2010). This result has opened the door for use of the short-wavelength response of COS, in particular the G140L mode, to perform spectroscopic observations at wavelengths inaccessible to previous *HST* instruments ($\lambda < 1130$ Å). See Appendix A of France et al. (2010) for preliminary work with this mode. The CALCOS pipeline processing of G140L segment B ($400 \text{ Å} \lesssim \lambda \lesssim 1175 \text{ Å}$) is not sufficiently mature to produce one-dimensional spectra appropriate for scientific analysis.

We therefore processed the data with a newer version of the CALCOS pipeline (v2.12), employing specially created reference files for flux and wavelength calibra-

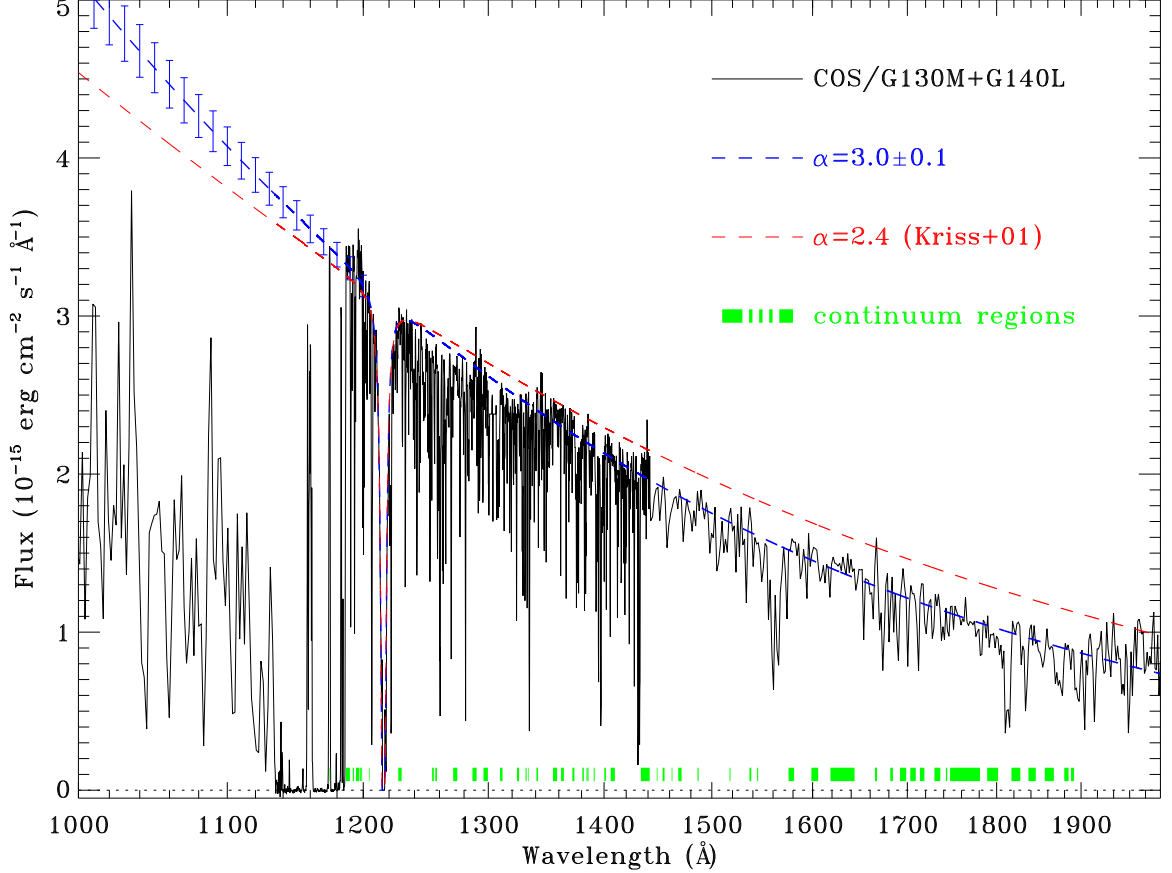


FIG. 1.— Overview of the COS/G130M and G140L data. Data are smoothed by 3 resolution elements and shown as observed (uncorrected) flux. The de-reddened data were fitted to a power law, $F_\lambda = F_0(\lambda/\lambda_0)^{-\alpha_s}$, with $\alpha_s = 3.0 \pm 0.1$. Error bars below $\lambda_0 = 1215 \text{ \AA}$ reflect $\pm 2\%$ uncertainty in continuum level and ± 0.1 uncertainty in α_s . This continuum is extrapolated below the HeII edge (1186 \AA) to derive HeII optical depths. Red curve shows continuum fit of Kriss et al. (2001) with $\alpha_s = 2.4$. Our steeper fit arises primarily from the higher quality COS data ($1200\text{--}2000 \text{ \AA}$) and, to lesser extent, from our larger adopted extinction, $E(B - V) = 0.022$ rather than 0.014 , extrapolated to the far-UV.

tions in the short-wavelength segment-B setting. The custom reference files that were created to supplement the CALCOS 2.12 release were a first-order dispersion solution for $\lambda < 1150 \text{ \AA}$ and a flux calibration curve. The wavelength calibration was created by fitting line centers to the pressure-broadened Lyman series lines observed in COS calibration spectra of white dwarfs (McCandliss et al. 2010). While G140L segment A uses a second-order polynomial wavelength solution, the relatively small amount of physical detector area used by G140L segment B allows a reasonable fit with a linear solution. We find a dispersion of $\Delta\lambda = -79.8 \text{ m\AA pixel}^{-1}$, and a long-wavelength zero-point of 1245.26 \AA . To align with G130M data, we shifted G140L-B wavelengths by $+3.9 \text{ \AA}$. For example, 1245.26 \AA (old G140L) becomes 1249.16 \AA (new G140L). The G140L-A wavelengths were shifted by only -0.4 \AA (~ 0.5 resolution element).

The calibration curve, translating count rate (counts s^{-1}) into flux ($\text{erg cm}^{-2} \text{ s}^{-1} \text{ \AA}^{-1}$) was created using the G140L segment-B effective area curve derived by McCandliss et al. (2010). We caution that there may still be significant uncertainty in this flux calibration. At $\lambda < 950 \text{ \AA}$, we should be within $\sim 50\%$

of the correct value. The accuracy is likely $\sim 20\text{--}25\%$ from $1025\text{--}1110 \text{ \AA}$ and $\sim 10\text{--}15\%$ from 1120 \AA onward. Continued testing of G140L-B observations will refine this calibration. This custom reduction produces reprocessed one- and two-dimensional spectral data products, which can be coadded following the procedure described above and in Danforth et al. (2010). The coadded data were used to create a low-resolution ($R \approx 10^3$, $\Delta\lambda \sim 1 \text{ \AA}$) spectrum of HE 2347–4342 at $\lambda \leq 1174 \text{ \AA}$. In principle, the COS/G140L wavelength coverage extends to very low wavelengths ($\sim 400 \text{ \AA}$). However, the combination of low instrumental effective area, $A_{\text{eff}} \sim 10 \text{ cm}^2$ at $\lambda \lesssim 1030 \text{ \AA}$ (McCandliss et al. 2010) and interstellar absorption by atomic and molecular hydrogen limit the working wavelength coverage. For the He II absorption toward HE 2347–4342, we present G140L data from $1030 \text{ \AA} \lesssim \lambda \leq 1174 \text{ \AA}$, corresponding to $z_{\text{HeII}} \approx 2.39\text{--}2.87$. We cross-calibrated the G140L segment-B spectrum with the short-wavelength data from G130M, finding that the flux calibration is better than 10% in the overlap region. The data were then used to extend our investigation of the He II ionization state in the IGM down to $z_{\text{HeII}} = 2.39$ (1030 \AA).

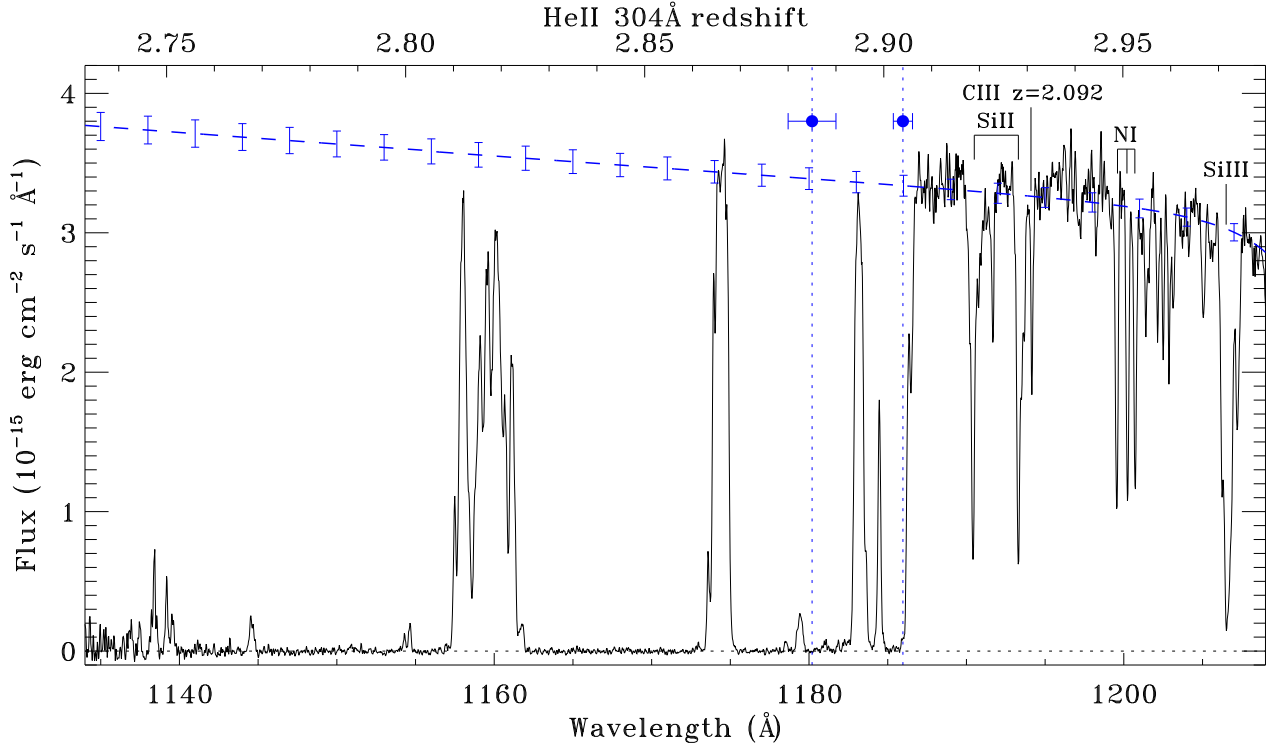


FIG. 2.— Detail of the G130M data showing HeII absorption and transmission windows. The two proposed QSO systemic redshifts ($z_{\text{QSO}} = 2.885$ and 2.904) and our extrapolated continuum are marked. Milky Way interstellar lines of NI, SiII, SiIII appear longward of 1190 \AA , and strong HeII absorption is seen shortward of 1186.26 \AA . We use the CIII ($z = 2.0921$) IGM absorption line to align the COS and VLT spectra. Windows of flux transmission appear at $1138, 1144, 1154, 1160, 1174, 1179, 1183$, and 1184 \AA . At 1174 \AA we see essentially 100% transmission, and yet we also observe three troughs of strong HeII absorption ($\tau_{\text{HeII}} \geq 5$) over large redshift intervals (and comoving radial distances) between $z = 2.751 - 2.807$ (61 Mpc), $z = 2.823 - 2.860$ (39 Mpc), and $z = 2.868 - 2.892$ (25 Mpc).

Figure 3 provides a comparison among three spectrographs: COS/G130M, COS/G140L, and *FUSE* (LiF1 and LiF2 channels). There is a fair amount of agreement in fluxes among these instruments, although the *FUSE* backgrounds at $1160\text{--}1187 \text{ \AA}$ are obviously incorrect. This comparison gives us confidence in using G140L data down to 1030 \AA .

3. RESULTS AND ANALYSIS

3.1. Systemic Redshift of QSO

The systemic redshift of HE 2347–4342 is of interest, both to fix the expected location of the He II edge and to infer the metagalactic radiation field from the QSO proximity effect (Dall’Aglio, Wisotzki, & Worseck 2008a,b). A significant puzzle for this sight line is the 6 \AA offset between the extent of strong He II absorption (out to 1186 \AA) and the expected He II edge (1180 \AA) based on an uncertain QSO emission-line redshift. Reimers et al. (1997) found $z_{\text{em}} = 2.885 \pm 0.005$, based on the weak O I $\lambda 1302$ emission line, while Scannapieco et al. (2006) quoted $z_{\text{em}} = 2.871$ with no error bar. Emission-line redshifts were also measured with UVES at the VLT/UT2 by Dall’Aglio et al. (2008b), who quoted $z_{\text{em}} = 2.886 \pm 0.003$ based on the O I + Si II blend and assuming a rest wavelength $\lambda_{\text{rest}} = 1305.77$ for the blend. Given the solar abundance ratio $(\text{O}/\text{Si})_{\odot} \approx 15$, this blend is probably dominated by three lines of O I, with a statis-

tically weighted centroid at 1303.49 \AA (Morton 2003). In total, the blend consists of three O I lines decaying to the ground-state fine-structure levels of O I [$(2p^3 3s)^3S_1 \rightarrow (2p^4)^3P_{2,1,0}$] at $1302.17, 1304.86, 1306.03 \text{ \AA}$ and two lines of Si II [$(3s 3p^2)^2S_{1/2} \rightarrow (3s^2 3p)^2P_{1/2,3/2}$] at 1304.37 and 1309.28 \AA . Dall’Aglio et al. (2008a) measured the redshifts of the strongest emission lines to be $z_{\text{em}} = 2.877 \pm 0.003$ (Ly α) and 2.861 ± 0.003 (C IV). However, there are well-known shifts in emission-line redshifts between the QSO systemic redshift and the “higher ionization lines” (e.g., Ly α , C III $\lambda 977$, C IV $\lambda 1549$). For instance, $1000\text{--}3000 \text{ km s}^{-1}$ offsets are commonly seen in the emission-line spectra of AGN (Espey et al. 1989; Corbin 1990). These issues provide systematic uncertainties in determining z_{em} , either from the weak O I/Si II blend or from higher ionization lines. Thus, the precise QSO systemic redshift remains uncertain.

Because of these problems with emission-line redshifts, we propose to use IGM absorption to determine the QSO redshift. We suggest that the QSO systemic redshift is $z_{\text{QSO}} = 2.904 \pm 0.002$ (Figure 4) based on the extent of the H I and He II absorption. This redshift is chosen as the midpoint between the centroid of the strong absorption feature seen in both H I and He II and the red edge of He II absorption. Figure 4 provides an overview of the COS/G130M spectrum from $1100\text{--}1190 \text{ \AA}$, together with a blowup of the region from 1173 \AA to the He II

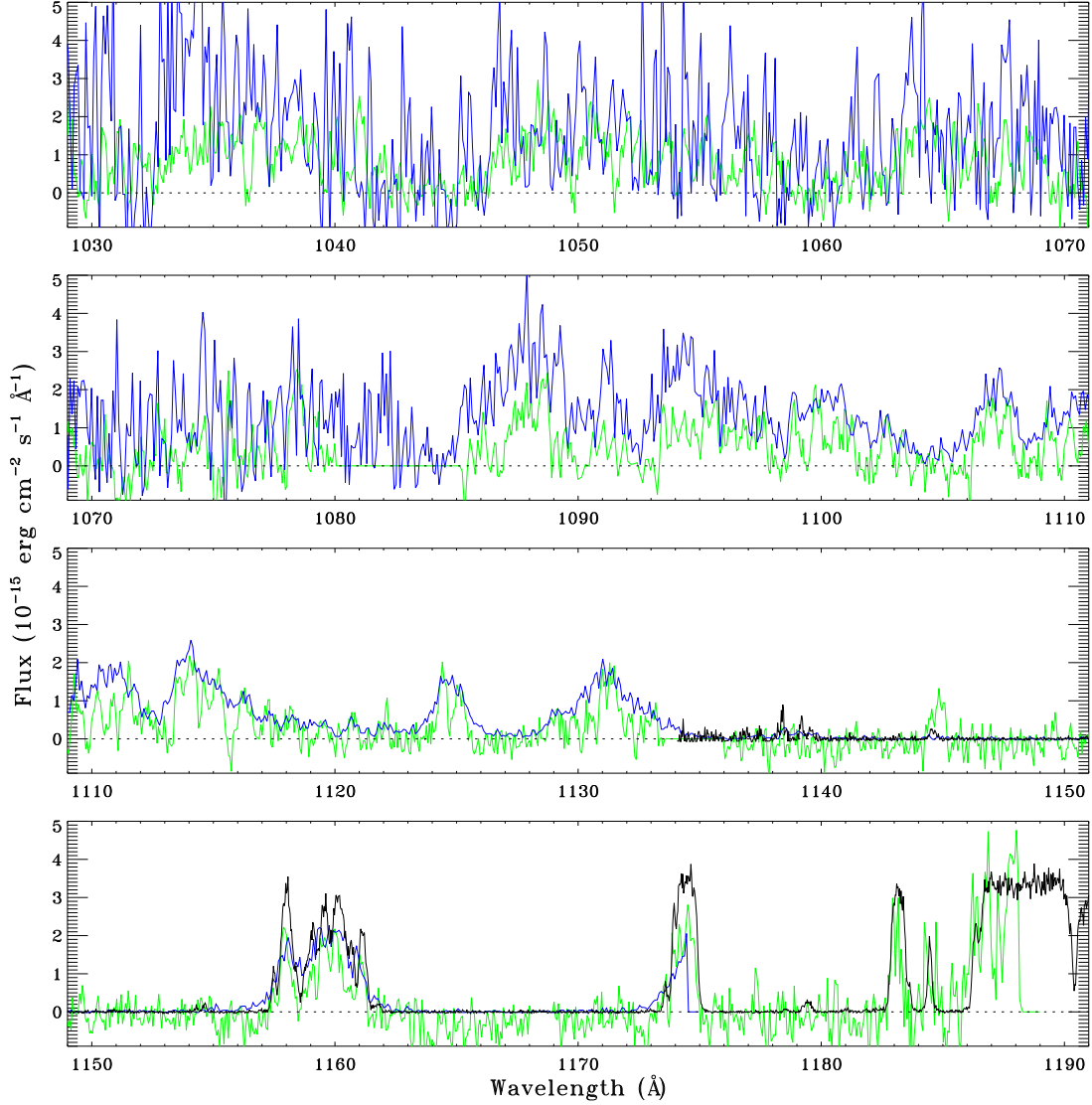


FIG. 3.— Comparison of the COS/G130M (black), COS/G140L (blue), and coadded *FUSE*/LiF1+LiF2 data (green). The COS/G130M data are binned by 3 pixels (half a resolution element). The *FUSE* data have been binned to one resolution element, and COS/G140L data are presented as observed (unbinned). The *FUSE* background solutions appear to be adequate at 1110–1150 Å, but poor between 1160–1187 Å. The flux and wavelength solutions for the two instruments are reasonably consistent, providing confidence in using G140L data at $\lambda > 1030$ Å.

edge near 1186 Å. We see absorption extending well beyond the wavelengths (1180.2–1180.5 Å) corresponding to the QSO emission-line redshifts, $z = 2.885 \pm 0.005$ and 2.886 ± 0.003 , suggested by Reimers et al. (1997) and Dall’Aglio et al. (2008b) respectively. The absorption between 1181–1186 Å suggests that the QSO actually lies at $z \approx 2.90$. Interestingly, we see no ionization effects from proximity to the QSO, a topic discussed further in Section 3.6.

The He II absorption profile shows an absorption feature at 1186.5 Å, with optical depth $\tau \approx 0.7$, equivalent width 95 mÅ, and FWHM = 0.14 Å. This may be proximate He II absorption or absorption from an intervening system. The spectrum near 1186.5 Å shows a clear flux minimum and recovery toward shorter wavelengths typical of weak absorption lines. A distinct He II absorber

would appear as a broader “shelf” on the side of the $\tau_{\text{HeII}} > 1$ trough. We do not make a specific line identification for the feature. It does not seem to be low-redshift Ly β nor any of the usual IGM metal-line systems (Danforth & Shull 2008).

Reimers et al. (1997) attribute the H I and He II absorption at $z > 2.885$ to a multicomponent system of associated absorbers between 1181–1186 Å (redshifts $z = 2.891$ to $z = 2.904$). Many of these systems have strong metal lines of C IV, N V, and O VI, and a few have anomalous ratios of He II and H I Ly α absorption. These observations suggest that the gas might be exposed to high fluxes of ionizing radiation and affected by nucleosynthetic anomalies in nuclear outflows. Smette et al. (2002) and Fechner et al. (2004) both noted evidence for “line-locking” in C IV and N V (although the latter group found no statistical evidence compared to simulated line

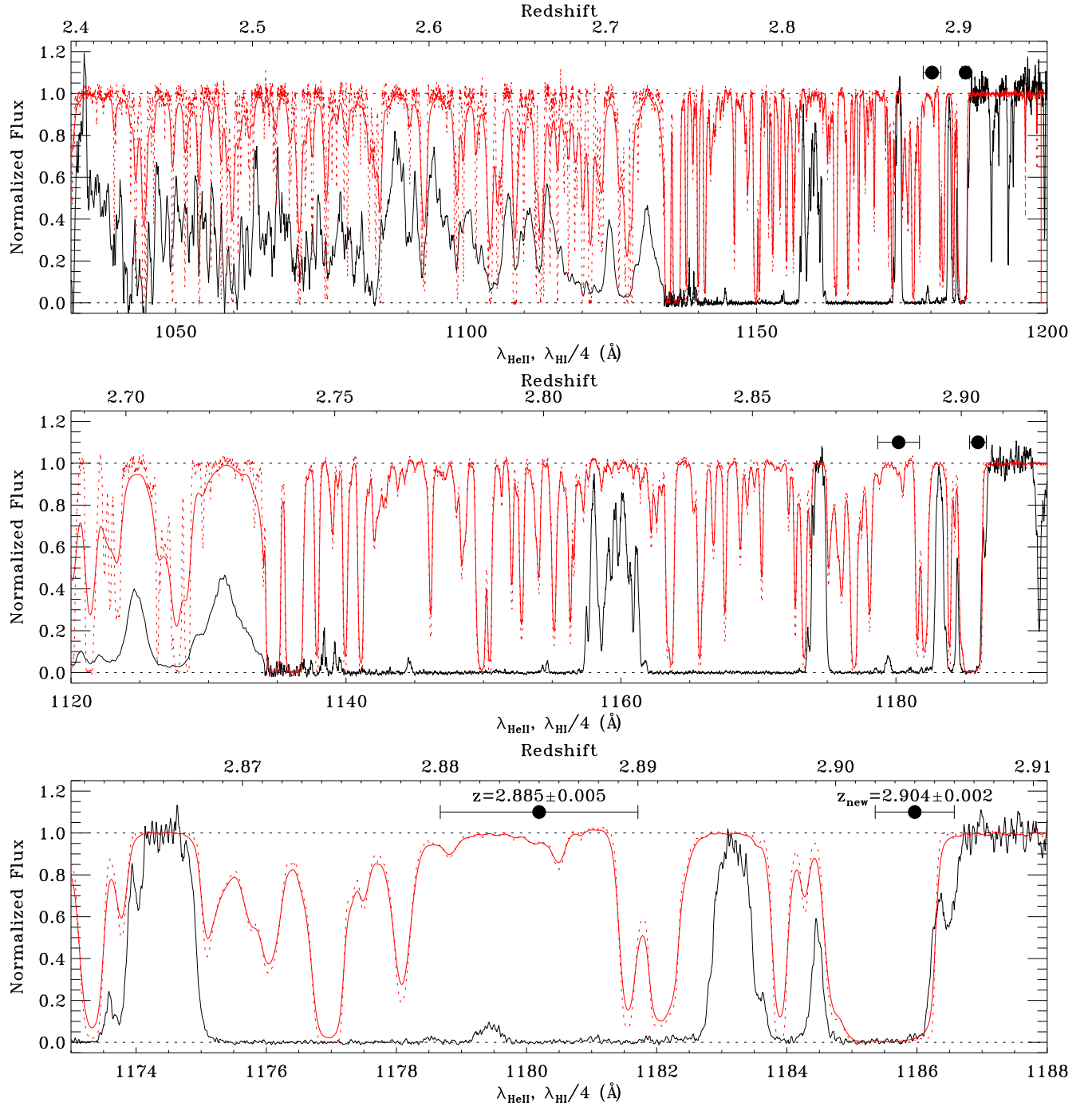


FIG. 4.— (Top Panel) Normalized COS/G130M and G140L flux (black) and VLT flux (red) vs. redshift ($z = 2.4 - 2.9$, top legend) and wavelength (bottom legend). HI wavelengths are divided by 4 for comparison with He II, and two proposed QSO redshifts are noted by filled black circles: $z_{\text{em}} = 2.885 \pm 0.005$ (Reimers et al. 1997) and $z = 2.904 \pm 0.002$ (this paper). Lower two panels show VLT/UVES data ($R = 44000$) from D. Reimers, convolved with COS line spread function to match COS resolution: $R = 18,000$ ($\lambda > 1134$ Å) and $R = 1800$ ($\lambda < 1134$ Å). Unconvolved HI data are shown by dotted red curves. Troughs of strong He II absorption (1175.2–1179.1 Å, 1179.5–1182.5 Å) are separated by small windows of flux transmission. Features at 1181–1186 Å are associated absorbers (Reimers et al. 1997), but with insufficient column density to block AGN ionizing flux.

lists). Line-locking occurs when two absorbers are separated by a velocity equal to the separation of the two doublet lines, resulting from radiation pressure on material physically near the QSO (Weymann, Carswell, & Smith 1981). These radiative forces will drive gas outward from the QSO, whereas the redshifted associated absorbers would have infall velocity $\sim 1500 \text{ km s}^{-1}$ relative to the QSO if $z_{\text{QSO}} = 2.885$. Thus, our proposed redshift, $z_{\text{QSO}} = 2.904$, provides a more plausible explanation.

The uncertainty in QSO systemic redshift illustrates the need for infrared observations. Unfortunately, the redshifted hydrogen Balmer lines fall in difficult spectral bands ($\text{H}\alpha$ at $2.563 \mu\text{m}$, $\text{H}\beta$ at $1.898 \mu\text{m}$), as does the $[\text{O II}] \lambda 3727$ doublet at 1.455 and $1.456 \mu\text{m}$. The forbidden lines of $[\text{O III}] \lambda 5007, 4959$ occur at more promising wavelengths, $1.955 \mu\text{m}$ and $1.936 \mu\text{m}$. Thus, infrared spectroscopic searches for the $[\text{O III}]$ forbidden lines may offer the best opportunity to resolve the issue of z_{QSO} .

3.2. Expected He II Gunn-Peterson Absorption

The standard GP optical-depth formula (Fan et al. 2006) for species ($i = \text{H I}$ or He II) is

$$\tau_i(z) = \left(\frac{\pi e^2}{m_e c} \right) \frac{\lambda_i f_i n_i}{H(z)}, \quad (1)$$

where $(\pi e^2/m_e c) = 2.654 \times 10^{-2} \text{ cm}^2 \text{ Hz}$ is the integrated classical oscillator cross section, $f_i = 0.4162$ is the absorption oscillator strength for $\text{Ly}\alpha$ transitions of H I and He II at rest wavelengths $\lambda_i = 1215.67 \text{ \AA}$ and 303.78 \AA , and n_i is their number density (cm^{-3}). The Hubble expansion parameter is $H(z) = H_0[\Omega_m(1+z)^3 + \Omega_\Lambda]^{1/2}$ in a flat Friedman cosmology ($\Omega_m + \Omega_\Lambda = 1$). All cosmological parameters and the resulting coefficients are based on WMAP-7 concordance values of CMB modeling from Komatsu et al. (2010), $\Omega_m h^2 = 0.1349 \pm 0.0036$, $\Omega_\Lambda = 0.728^{+0.015}_{-0.016}$, and $\Omega_b h^2 = 0.02260 \pm 0.00053$, and Hubble constant $H_0 = (100 \text{ km s}^{-1} \text{ Mpc}^{-1})h$ with $h = 0.70$. To set the ion densities n_i , we define x_{HI} and x_{HeII} as the abundance fractions of H I and He II , respectively. (The quantity x_{HI} is often called the neutral fraction.) The factors δ_i are the overdensities of H (at $z \approx 6$) and He (at $z \approx 3$) relative to the mean co-moving baryon density, $\langle \rho_b \rangle = (\Omega_b \rho_{\text{cr}}) = 4.25 \times 10^{-31} \text{ g cm}^{-3}$. With a primordial helium abundance $Y = 0.2477 \pm 0.0029$ by mass (Peimbert et al. 2007) and $y = (Y/4)/(1-Y) = 0.0823$ by number, this baryon density corresponds to H I and He II number densities,

$$n_{\text{HI}} = (6.55 \times 10^{-5} \text{ cm}^{-3}) x_{\text{HI}} \delta_{\text{H}} \left[\frac{(1+z)}{7} \right]^3, \quad (2)$$

$$n_{\text{HeII}} = (1.01 \times 10^{-6} \text{ cm}^{-3}) x_{\text{HeII}} \delta_{\text{He}} \left[\frac{(1+z)}{4} \right]^3. \quad (3)$$

In the high- z limit, $\Omega_m(1+z)^3 \gg \Omega_\Lambda$, we can express the Hubble parameter as $H(z) \approx H_0 \Omega_m^{1/2} (1+z)^{3/2} \approx (294 \text{ km s}^{-1} \text{ Mpc}^{-1})[(1+z)/4]^{3/2}$ scaled to the epoch $z \approx 3$ relevant for the beginning of He II reionization.

Thus, the Gunn-Peterson optical depths for H I (scaled to the $z = 6$ epoch) and He II (scaled to the $z = 3$ epoch)

are:

$$\tau_{\text{HI}}(z) = (3.99 \times 10^5) \left[\frac{(1+z)}{7} \right]^{3/2} x_{\text{HI}} \delta_{\text{H}}, \quad (4)$$

$$\tau_{\text{HeII}}(z) = (3.55 \times 10^3) \left[\frac{(1+z)}{4} \right]^{3/2} x_{\text{HeII}} \delta_{\text{HeII}}. \quad (5)$$

Very small abundance fractions, $x_{\text{HI}} \approx 10^{-4}$ and $x_{\text{HeII}} \approx 10^{-2}$, will saturate the Gunn-Peterson $\text{Ly}\alpha$ absorption in H I and He II , with optical depths $\tau_i \gg 10$, even in under-dense regions with $\delta_i = 0.1$. It is primarily for this reason that the hydrogen reionization epoch is so difficult to measure in $\text{Ly}\alpha$ absorption at $z \geq 6$ (Fan et al. 2006). However, He II absorption at $z \leq 3$ can probe 50–100 times higher abundance fractions in x_{HeII} . For the maximum observable values of He II optical depth ($\tau_{\text{HeII}} = 5$) and with typical densities in low-density filaments and voids, the intervals of high He II absorption at $z = 2.8 \pm 0.1$ correspond to He II fractions,

$$x_{\text{HeII}} = (0.015) \left[\frac{\tau_{\text{HeII}}}{5} \right] \left[\frac{(1+z)}{3.8} \right]^{-3/2} \left[\frac{\delta_{\text{He}}}{0.1} \right]^{-1}. \quad (6)$$

These overdensities, $\delta_{\text{He}} = 0.1$, are appropriate for the low-column-density ($\log N_{\text{HI}} \leq 13.5$) regions of the $\text{Ly}\alpha$ forest.

Figure 5 shows the He II optical depths for $2.4 < z < 2.9$, using COS data from both G140L and G130M and *FUSE*. To construct this figure, we reconstructed “horizontal error bars” representing the redshift bins (Δz) used in these papers. We used unpublished Δz and uncertainties in optical depths τ_{HeII} from Shull et al. (2004). From Zheng et al. (2004), we used values of Δz and τ_{HeII} from their Figure 3, with 25% uncertainties in τ_{HeII} . We find reasonable agreement with the *FUSE* optical depths (Shull et al. 2004) down to $z = 2.4$, although some of the G140L fluxes are higher than those in the *FUSE* extension to $z \leq 2.4$ (Zheng et al. 2004). The smaller *FUSE* optical depths may arise from uncertain background subtractions. Defining the redshift ranges for these data points is difficult for optical depths that vary rapidly over $\Delta z \approx 0.01$.

Future COS spectra of fainter He II -GP targets (often 19th magnitude AGN) will have low S/N ratios and will probably not show the fluctuations in optical depths found here. At best, they will measure broad-band optical depths, $\langle \tau_{\text{HeII}} \rangle$. For HE 2347–4342, we list below the He II and H I optical depths averaged over $\Delta z = 0.1$ windows, together with the standard deviations of their distributions:

- ($z = 2.4\text{--}2.5$) $\langle \tau_{\text{HI}} \rangle = 0.12^{+0.21}_{-0.09}$, $\langle \tau_{\text{HeII}} \rangle = 1.11^{+0.97}_{-0.49}$
- ($z = 2.5\text{--}2.6$) $\langle \tau_{\text{HI}} \rangle = 0.12^{+0.25}_{-0.08}$, $\langle \tau_{\text{HeII}} \rangle = 1.18^{+0.71}_{-0.50}$
- ($z = 2.6\text{--}2.7$) $\langle \tau_{\text{HI}} \rangle = 0.26^{+0.36}_{-0.18}$, $\langle \tau_{\text{HeII}} \rangle = 1.37^{+1.03}_{-0.53}$

There may be a slight trend to higher η at lower redshifts, as we discuss in Section 3.4. Considering the ratios of the broad-band averages, we find that $\langle \eta \rangle$ rises from 21^{+33}_{-17} at $z = 2.6\text{--}2.7$ to values 39^{+84}_{-31} at $z = 2.5\text{--}2.6$ and 37^{+72}_{-34} at $z = 2.4\text{--}2.5$. Despite the large spreads of the optical-depth distributions, the means are fairly well determined.

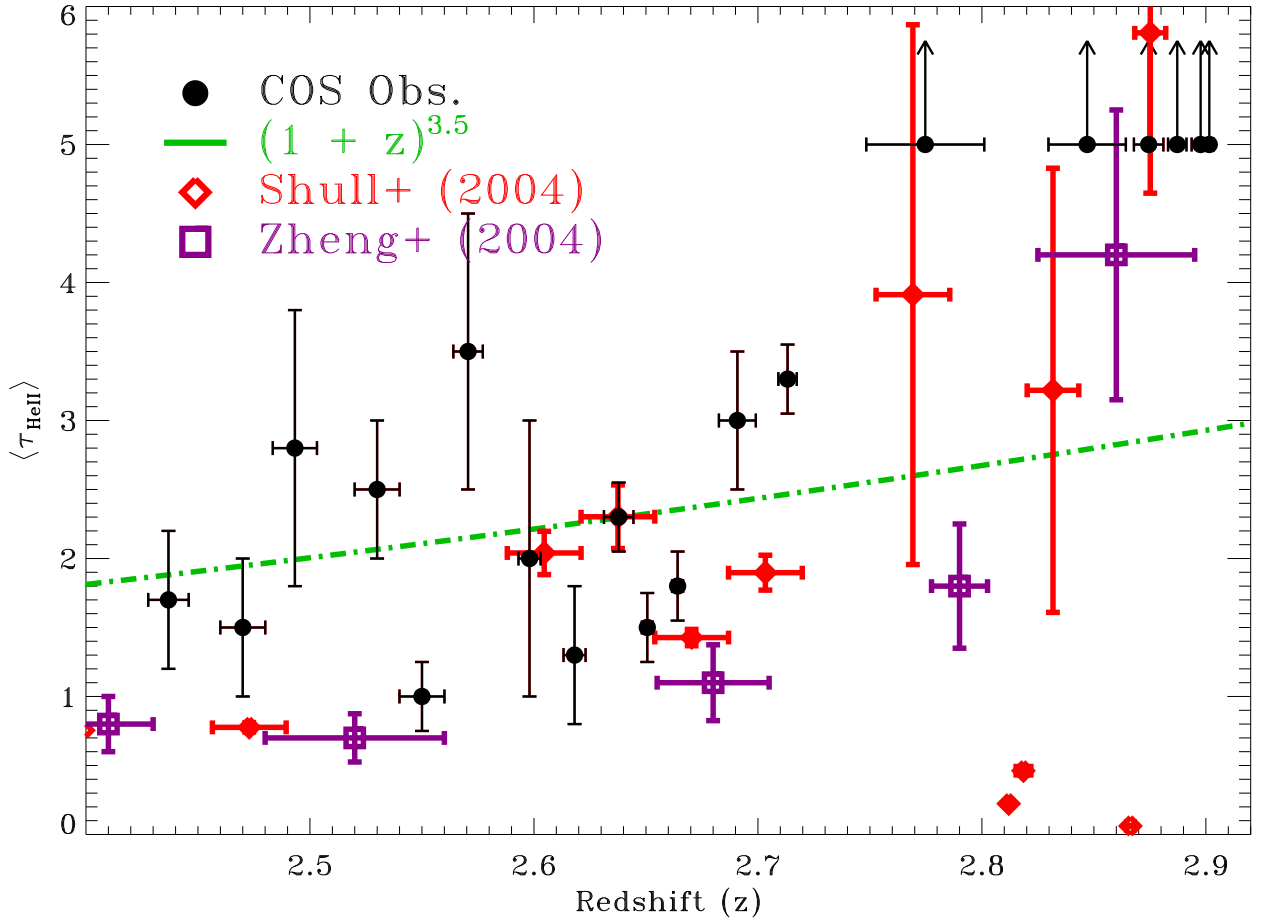


FIG. 5.— Absorption optical depths, τ_{HeII} , vs. redshift (bins listed in Table 2) for this paper (black points: COS G130M and G140L) and from previous *FUSE* measurements (Zheng et al. 2004; Shull et al. 2004). COS optical depths are generally higher than those found by *FUSE*. Theoretically predicted $(1+z)^{3.5}$ redshift scaling (Fardal et al. 1998) is shown as a dotted line. High COS optical depths, $\tau_{\text{HeII}} \geq 5$, are plotted as lower limits, based on zero-level flux accuracy implied by RMS variations, $\sigma_F = 2.7 \times 10^{-17}$ ergs cm $^{-2}$ s $^{-1}$ Å $^{-1}$, at the bottom of troughs at 1145–1155 Å and 1162–1173 Å.

Figure 6 shows examples of the He II and H I ionization structures found in our cosmological simulations (Smith et al. 2010), computed with *Enzo*, an N-body, hydrodynamical code modified to compute time-dependent H and He ionization. One can see the projected topology of the cosmic web, the baryon overdensity, the ionization fractions of H I and He II at $z = 2 - 3$, and their ratio, $x_{\text{HeII}}/x_{\text{HI}}$. Observationally, we measure the ratio of column densities, $\eta = N(\text{He II})/N(\text{H I})$, which we approximate as $\eta \approx 4\tau_{\text{HeII}}/\tau_{\text{HI}}$. The factor of 4 arises from the larger He II frequency bandwidth, with the absorption-line cross section, $\sigma_\lambda \propto f\lambda$, scaling as oscillator strength times wavelength. Our IGM simulations at $z \approx 2.5$ show a mean value of the ionization ratio, $x_{\text{HeII}}/x_{\text{HI}} \approx 500$, corresponding to $\langle \eta \rangle \approx 40$ for primordial He/H = 0.0823 by number. We have confirmed that a substantial amount of observable He II, with $x_{\text{HeII}} = 0.001 - 0.01$, comes from ionized gas with $\log T = 4.0 - 5.3$ (much of it at $\log T = 4.3$) and $\log \delta_H = -1$ to $+2$. This He II gas is primarily confined to photoionized filaments in the cosmic web, with some contribution from collisional ionization (at $T > 10^5$ K). Further analysis of

these simulations will appear in a later paper.

3.3. He II and H I Optical-Depth Ratios

The H I and He II Ly α -forest absorbers have traditionally been assumed to arise in photoionized gas, irradiated by metagalactic ionizing (EUV) radiation of specific intensity $J_\nu = J_i(\nu/\nu_i)^{-\alpha_s}$, where i refers to H I ($h\nu_i = 13.6$ eV) or He II ($h\nu_i = 54.4$ eV). For these hydrogenic species, whose photoionization cross sections above threshold $h\nu_i$ scale as $\sigma_\nu = \sigma_i(\nu/\nu_i)^{-3}$, the photoionization rates $\Gamma_i = (4\pi\sigma_i/h)J_i/(\alpha_i + 3)$. The parameters α_i are local spectral indices of the ionizing background at 1 ryd and 4 ryd, respectively, and provide minor corrections to the photoionization rates. For typical metagalactic fluxes and IGM densities during reionization, hydrogen and helium are mostly ionized, with fractions $x_{\text{HI}} \ll x_{\text{HII}}$ and $x_{\text{HeI}} \ll x_{\text{HeII}} \ll x_{\text{HeIII}}$. Because the first ionization potentials of H I (13.6 eV) and He I (24.58 eV) are not greatly disparate, we expect the He III and H II ionization fronts to coincide for appropriate values of ionizing spectral index. For QSO ionizing spectra of power-law form, the He II and H I ionization fronts,

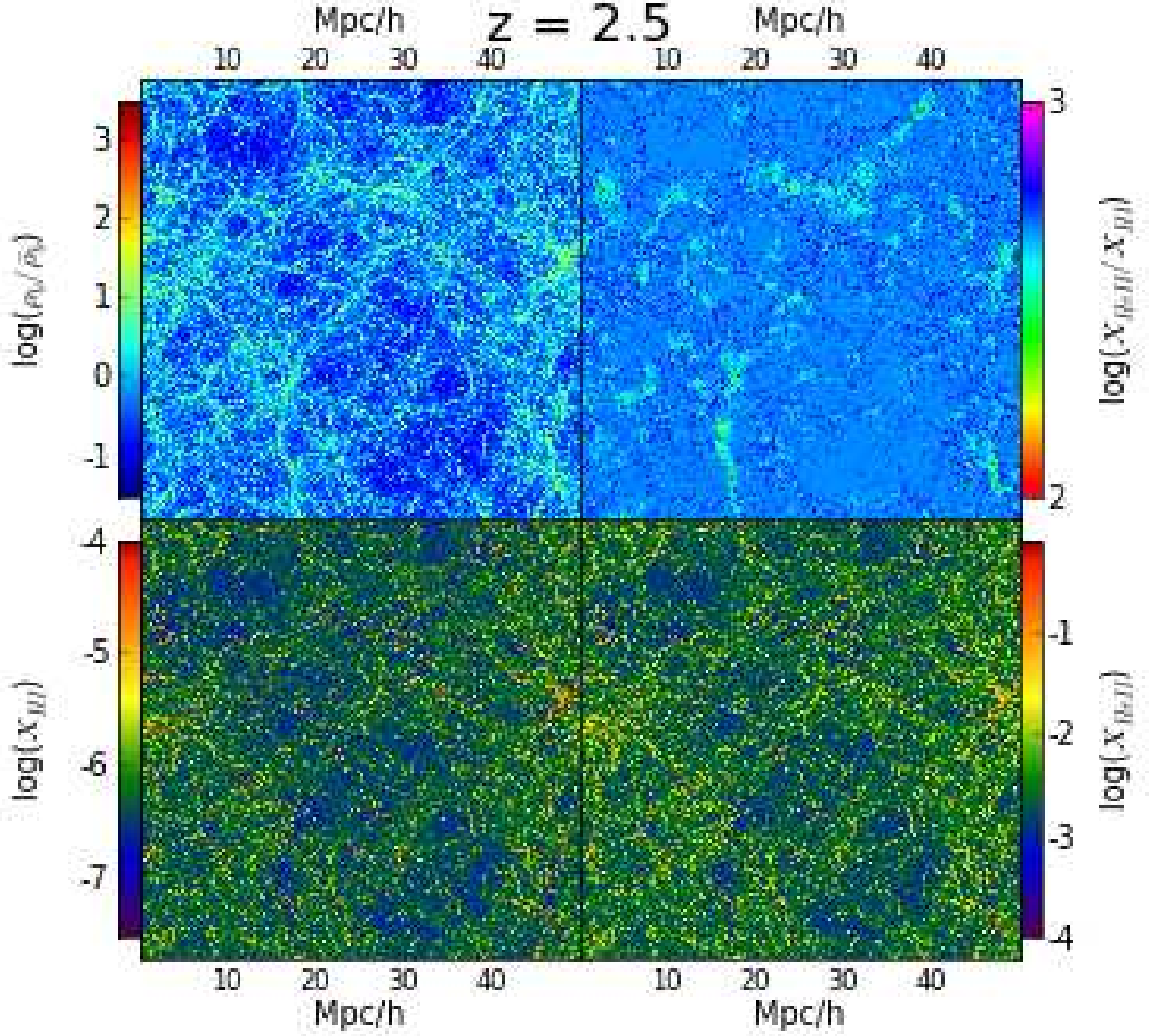


FIG. 6.— Four-panel plot of results from our IGM simulations at $z = 2.5$ (Smith et al. 2010) showing baryon overdensity (top left), ionization fractions of H I and He II (bottom left and right), and their ratio $x_{\text{HeII}}/x_{\text{HI}}$ (top right). Filamentary structures in the cosmic web are obvious in both top panels, with a mean value, $\langle x_{\text{HeII}}/x_{\text{HI}} \rangle \approx 500$, corresponding to $\eta = n_{\text{HeII}}/n_{\text{HI}} \approx 40$ for primordial He/H = $y = 0.0823$. Much of the He II in these filaments appears to be photoionized gas at $10^{4.3}$ K, but with some contribution from collisional ionization at $T > 10^5$ K. **Original paper with higher resolution available at <http://casa.colorado.edu/~mshull/HeII-paper.pdf>**

driven by the photon fluxes at 1 ryd and 4 ryd, respectively, will propagate at the same (photon flux-limited) velocity for a critical spectral index,

$$\alpha_{\text{crit}} = -\frac{(\ln y)}{\ln 4} \approx 1.80, \quad (7)$$

corresponding to our adopted He/H abundance, $y = 0.0823$. The agreement with the *HST*-observed mean spectral index of AGN at 1–2 ryd, $\langle \alpha_s \rangle = 1.76 \pm 0.12$ (Telfer et al. 2002), suggests that H II and He III ionization fronts normally propagate together.

In photoionization equilibrium in regions of high ionization, $x_{\text{HI}} \ll 1$ and $x_{\text{HeII}} \ll 1$, the He II/H I abundance

ratio is (Fardal et al. 1998; Shull et al. 2004),

$$\begin{aligned} \eta \equiv \frac{N_{\text{HeII}}}{N_{\text{HI}}} &\approx \frac{n_{\text{HeIII}}}{n_{\text{HII}}} \frac{\alpha_{\text{HeII}}^{(A)}}{\alpha_{\text{HI}}^{(A)}} \frac{\Gamma_{\text{HI}}}{\Gamma_{\text{HeII}}} \\ &\approx (1.77) \frac{J_{\text{HI}}}{J_{\text{HeII}}} \frac{(3 + \alpha_{\text{HeII}})}{(3 + \alpha_{\text{HI}})} T_{4.3}^{0.042}. \end{aligned} \quad (8)$$

The numerical coefficient has been increased from 1.70 to 1.77, reflecting an updated value of the primordial He/H abundance, $y = 0.0823$, which we use as an approximation to $n_{\text{HeIII}}/n_{\text{HII}}$. In this equation, $\alpha_{\text{HI}}^{(A)}$, $\alpha_{\text{HeII}}^{(A)}$, Γ_{HI} , and Γ_{HeII} are the case-A recombination rate coefficients.

cients and photoionization rates for H I and He II, and J_{HI} and J_{HeII} are the specific intensities of the ionizing radiation field at 1 ryd and 4 ryd. The parameter $T_{4.3} = (T/10^{4.3} \text{ K})$ is used to scale the temperature dependence of the Case-A recombination rates over the range $T = 10,000 \text{ K}$ to $20,000 \text{ K}$ (Osterbrock & Ferland 2006): $\alpha_{\text{HeII}}^{(A)} \approx (1.36 \times 10^{-12} \text{ cm}^3 \text{ s}^{-1}) T_{4.3}^{-0.694}$ and $\alpha_{\text{HI}}^{(A)} \approx (2.51 \times 10^{-13} \text{ cm}^3 \text{ s}^{-1}) T_{4.3}^{-0.736}$.

Equation (8) is an approximation, which will break down when x_{HeII} becomes significant. It also does not include the effects of collisional ionization of He II, which can become important in the shocked filaments of shocked gas at $T > 10^5 \text{ K}$, the so-called warm-hot intergalactic medium (WHIM). As noted in Figure 6, our simulations suggest that some of the He II in shocked IGM filaments may be collisionally ionized gas at $T > 10^5 \text{ K}$. However, the bulk of the He II is photoionized gas at $T \approx 10^{4.3 \pm 0.3} \text{ K}$.

3.4. Troughs of Strong He II Absorption

As shown in Figures 2 and 4, we have confirmed the presence of three long troughs with strong He II absorption ($\tau_{\text{HeII}} \gtrsim 5$) and no detectable flux. These troughs have been noted previously (Reimers et al. 1997; Smette et al. 2002; Shull et al. 2004), but the very low COS backgrounds allow us to better characterize their optical depth. We also detect numerous windows of flux transmission (e.g., at 1138, 1139, 1144, 1154, 1160, 1174, and 1179 Å – see Figure 2). The G130M data provide accurate boundaries in redshift. From those, we can determine their comoving radial sizes, using WMAP-7 cosmological parameters:

1. (*Trough 1*) $z = 2.751 - 2.807$ (61 Mpc),
2. (*Trough 2*) $z = 2.823 - 2.860$ (39 Mpc),
3. (*Trough 3*) $z = 2.868 - 2.892$ (25 Mpc).

These dimensions, all much larger than 10 Mpc, are incompatible with zones of photoionization around typical QSOs. They are also unlikely to exist at the epoch following the overlap of expanding cosmological I-fronts. Recent theoretical modeling has studied the statistics of He II troughs (McQuinn et al. 2009; McQuinn 2009; Furlanetto 2009a,b; Dixon & Furlanetto 2009). These studies examine large-scale fluctuations in the He II Ly α forest transmission, during and after He II reionization. A robust result is that long troughs of large optical depth, $\tau_{\text{HeII}} > 4$, cannot be explained in models with a smoothly evolving ionizing radiation field (Furlanetto & Dixon 2010). Furthermore, the observed 25–60 Mpc troughs of high He II opacity between $2.751 < z < 2.892$ cannot be accommodated in standard reionization models unless He II reionization is delayed until $z < 2.7$. The He II absorption is therefore expected to be patchy at $z \gtrsim 2.7$, as we have observed.

It would be useful to conduct surveys (Worseck et al. 2007) of galaxies and QSOs near the sight line at these trough redshifts to identify potential sources of ionization (or lack thereof). As discussed in Section 3.2, the He II opacity greatly exceeds that of H I; the ratio $\eta \gg 1$ for typical conditions in an IGM photoionized by QSOs of low space density. Thus, the propagation and overlap of

I-fronts driven by He II ionizing continua will likely differ from those of hydrogen. The greater He II opacity means that filaments of the cosmic web still have $\tau_{\text{HeII}} = 2 - 3$ at $z = 2.4 - 2.7$ (see Figures 5 and 6). Thus, the topology of overlapping He III ionized zones probably differs from that of merging H II regions at $z = 6$. These theoretical results are explored in a later paper (Smith et al. 2010) using adaptive-mesh cosmological simulations with the *Enzo* code.

3.5. Fluctuations in He II/H I Ratios.

Because reionization involves the stochastic propagation and overlap of ionization fronts (I-fronts), one naturally expects variations in the abundances of H I and He II. The metagalactic flux of high-energy (4 ryd continuum) radiation varies primarily because of the low space density of the dominant ionizing sources (AGN) and varying attenuation through the IGM. The variations in He II opacity can be especially large during reionization, because the 4 ryd continuum is strong near AGN (inside the I-fronts) but heavily attenuated in the He II troughs, far from the AGN and within the gaseous filaments of the cosmic web.

Figure 4 shows both He II and H I absorption, overlaid in redshift, illustrating the correspondence of He II flux-transmission windows with weak spots (low H I absorption) in the H I Ly α forest. The non-Gaussian wings in the COS line-spread function (LSF) is most significant for weak absorbers, but we believe this is completely accounted for in the convolution of the H I data by the COS LSF. The resolving power ($R = 18,000$) of the COS LSF is more appropriately the effective Gaussian resolving power (Green et al. 2010). The main difference in the convolved and unconvolved H I data in Figure 4 is simply a degradation in resolution by a factor of 2.5. The COS LSF contributes to a redistribution of flux in the narrowest lines, but this is accounted for with the non-Gaussian LSF.

The He II/H I ratio, $\eta \approx 4\tau_{\text{HeII}}/\tau_{\text{HI}}$, tracks the ratio of ionizing fluxes at 1 and 4 ryd (see equation [8]). Table 3 presents the mean and median values of η in the G130M and G140L data, and over various redshifts. In different columns, we present these statistics for the G140L and G130M spectral regions, and for the region ($2.73 < z < 2.87$) where the two gratings overlap. To calculate $\eta(z)$, we convolve the high-resolution VLT data with either the medium-resolution (G130M) or low-resolution (G140L) COS line-spread functions, depending which dataset is representing He II at a particular redshift. The COS data are then smoothed by seven pixels (~ 1 resolution element) and up-sampled to the finer VLT wavelength scale. Optical depths $\tau_{\text{HeII}}(z)$ and $\tau_{\text{HI}}(z)$ are calculated on a pixel-by-pixel basis.

Figures 7 and 8 show $\tau(z)$ and $\eta(z)$ and demonstrate that He II optical depth saturates in certain regions. Over the range $2.4 < z < 2.9$, 32% of pixels are saturated, but this fraction depends strongly on redshift and spectral resolution. In the low-resolution data at $z < 2.73$, we find that τ_{HeII} is almost always unsaturated. At $z > 2.7$, we see long absorption troughs in which 40–45% of the pixels have $\tau_{\text{HeII}} > 5$. We computed mean and median values of η using both saturated and unsaturated pixels. As the saturated pixel values for He II are entirely in the numerator, our average η values

TABLE 3
STATISTICS OF HE II/HI COLUMN-DENSITY RATIOS ^a

Statistic	G140L ($2.4 < z < 2.73$) Low-Res'n	G130M ($z > 2.73$) Medium Res'n	G140L ($2.73 < z < 2.87$) Overlap Region	G130M ($2.73 < z < 2.87$) Overlap Region
Mean (η)	47 ± 42	209 ± 281	105 ± 121	208 ± 281
Median (η)	33^{+56}_{-19}	88^{+391}_{-71}	69^{+94}_{-41}	87^{+388}_{-71}
Mean ($\log \eta$)	1.52 ± 0.38	1.90 ± 0.68	1.83 ± 0.41	1.89 ± 0.68
Median ($\log \eta$)	$1.51^{+0.43}_{-0.39}$	1.94 ± 0.74	1.84 ± 0.38	1.94 ± 0.74

^a We list mean and median values of the ratio $\eta \equiv N_{\text{HeII}}/N_{\text{HI}}$ over redshift ranges covered at low resolution (G140L) and medium resolution (G130M). The last two columns show η statistics for the overlap range, $2.73 < z < 2.87$. All statistics are calculated including both saturated and unsaturated values of τ_{HeII} . Using only unsaturated pixels reduces $\langle \eta \rangle$ by 10–20% at $z > 2.7$, with no change at $z < 2.7$.

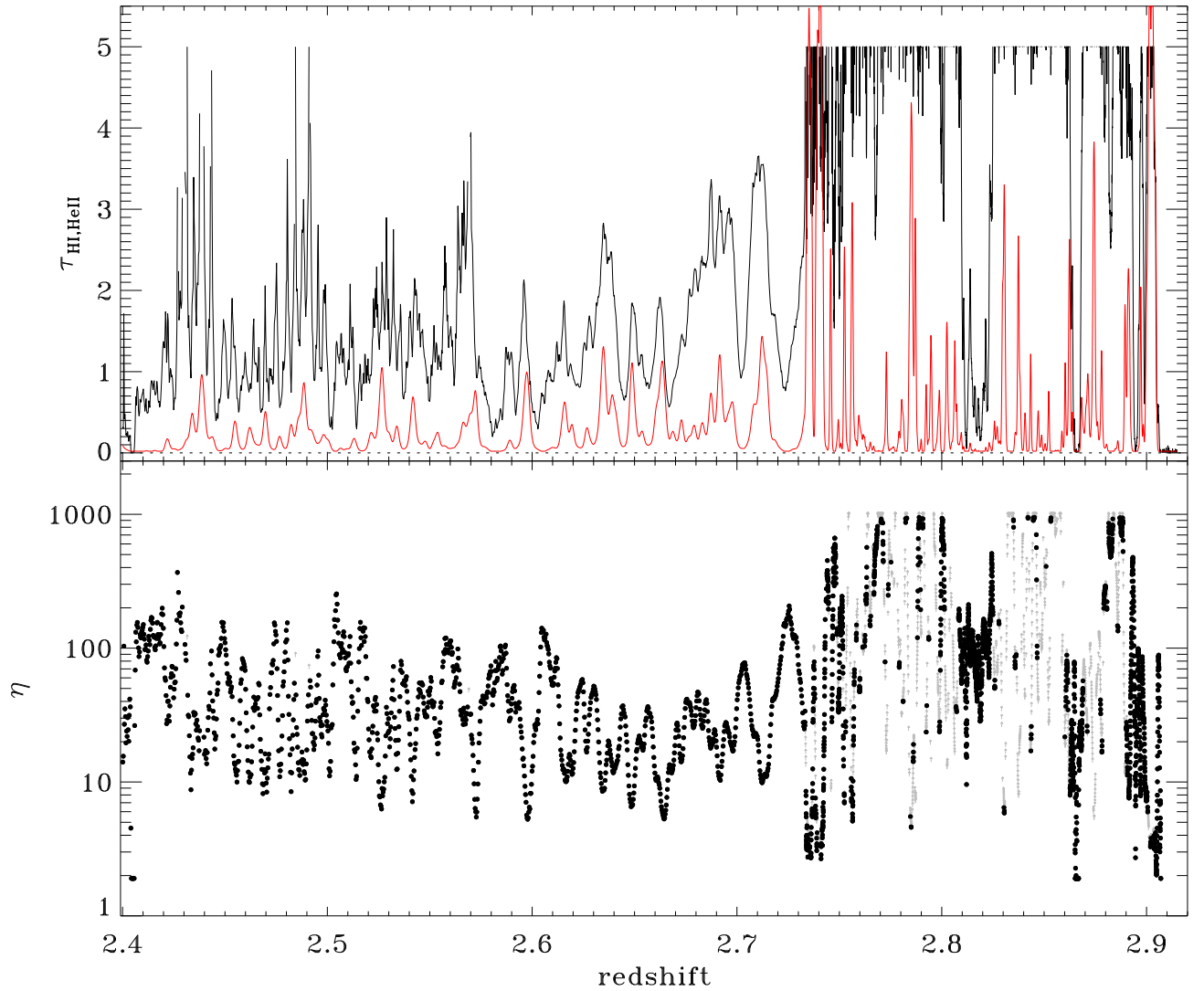


FIG. 7.— Optical depth for HeII (black) and HI (red) and their ratio, $\eta \approx 4\tau_{\text{HeII}}/\tau_{\text{HI}}$, versus redshift. Note the change in spectral resolution at $z < 2.73$, the transition between G130M and G140L gratings. The VLT/UVES data have been convolved with the appropriate COS line spread function. We only plot values $\tau_{\text{HeII}} \leq 5$. Fluctuations at $\Delta z \approx 0.01$ correspond to proper distances of 10.8 Mpc at $z = 2.8$. For our detectable ranges of optical depth ($0.02 \leq \tau_{\text{HeII}} < 5$ and $0.01 < \tau_{\text{HI}} < 5.5$) we believe η can be determined reliably over the range $5 < \eta < 500$ (G130M) and $10 < \eta < 100$ (G140L). The mean values and standard deviations are $\langle \eta \rangle = 47 \pm 42$ (for G140L range) and $\langle \eta \rangle = 189 \pm 276$ (for G130M range). See full statistics in Table 3. There may be a slight trend of higher η toward lower z .

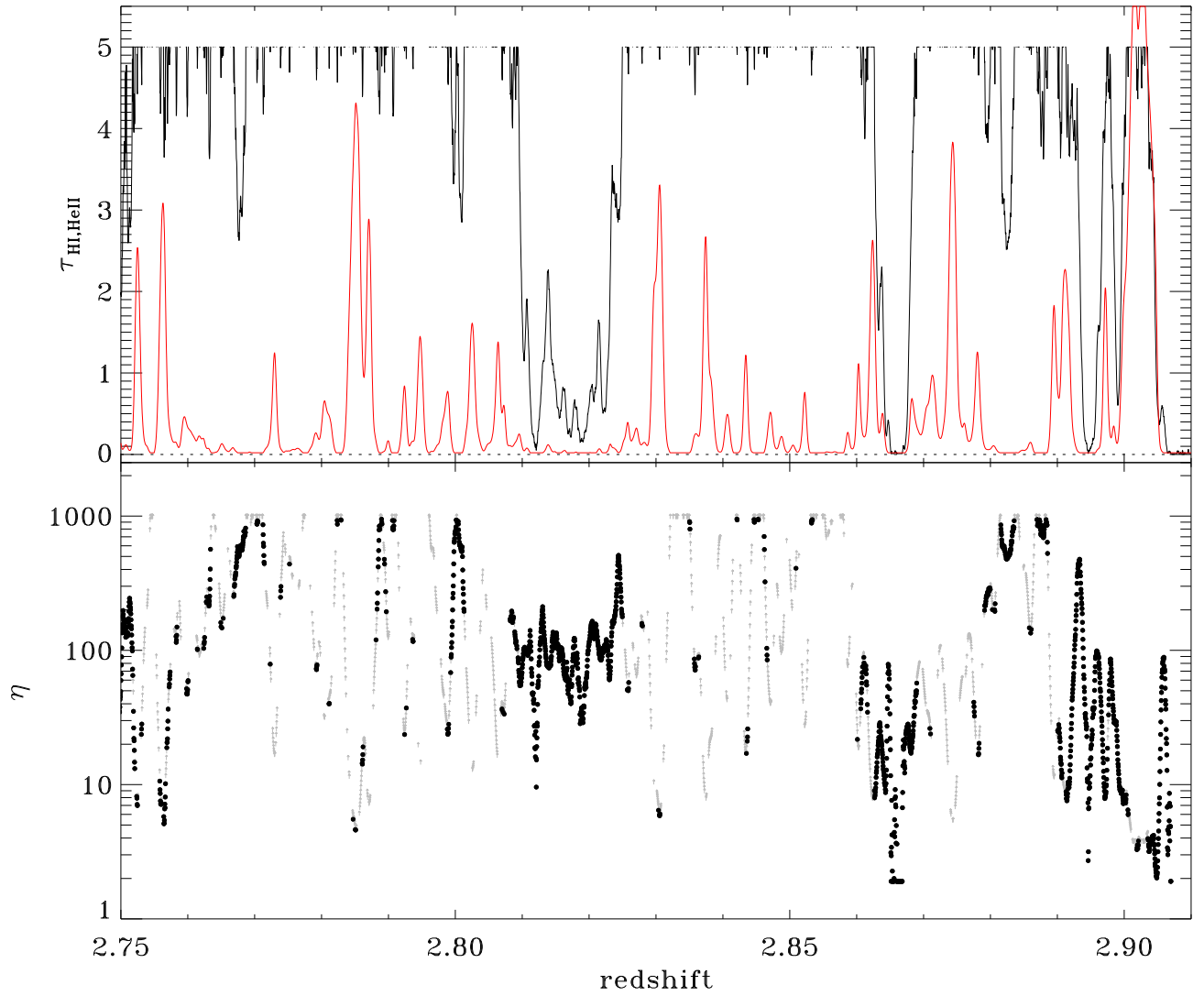


FIG. 8.— Closeup of optical depth for HeII (black) and HI (red) and their ratio η at redshifts near the QSO, $2.75 \leq z \leq 2.90$. In the higher-resolution G130M data, η varies on scales down to $\Delta z \approx 0.003$. Grey points indicate locations where $\tau_{\text{HeII}} \geq 5$, so that η is a lower limit. We believe η can reliably be measured over the range $5 < \eta < 500$, considering reasonable limits on $0.02 < \tau_{\text{HeII}} < 5$ and $0.01 < \tau_{\text{HI}} < 5.5$.

are lower limits. Using only unsaturated pixels reduces $\langle \eta \rangle$ systematically by 10-20% at $z > 2.7$. Correcting for larger true values of $\tau_{\text{HeII}} > 5$ would increase the mean statistics. There is no change at $z < 2.7$.

We confirm the fluctuations seen by *FUSE* between $2.73 < z < 2.90$ (Kriss et al. 2001; Shull et al. 2004) on small scales, $\Delta z \approx 0.003 - 0.01$. Figures 7 and 8 show that η fluctuates on scales down to $\Delta z \approx 0.01$ at G140L resolution and $\Delta z \approx 0.003$ at G130M resolution. For reference, the redshift interval $\Delta z = 0.01$ corresponds to a comoving radial distance of 10.8 Mpc at $z = 2.8$. Regions of hot gas ($T > 10^5$ K) might appear as high- η systems, in which H I is far more collisionally ionized than He II. However, the COS data also exhibit several instances of low- η absorbers with $\eta \approx 5 - 20$. Since $\eta \approx 4\tau_{\text{HeII}}/\tau_{\text{HI}}$, the low- η systems appear primarily where the H I optical depth is large and He II optical depth small. If photoionized, these absorbers may be irradiated by very hard radiation fields, with large ratios of $J_{\text{HeII}}/J_{\text{HI}}$ (equation 8), perhaps near an AGN with a particularly flat EUV spectral index, $\alpha_s < 1$.

Several good examples of low- η absorbers appear at $z \approx 2.755, 2.785, 2.830, 2.865$, and 2.904 . Most of these systems have high τ_{HI} , the exception being the absorber at $z = 2.865$ in which both τ_{HeII} and τ_{HI} are low, and their ratio poorly determined. For high- η systems, the G130M data exhibit regions with $\eta = 200 - 500$, typically in gas with large τ_{HeII} but low τ_{HI} . Extreme excursions in η may arise from noise, and their detectable range depends on spectral resolution. We therefore take care to assess the range over which we can measure reliable optical depths. For ratios within the range $\eta = 10 - 100$ (G140L) and $\eta = 5 - 500$ (G130M), we believe nearly all the fluctuations are real. Unfortunately, strong troughs of He II absorption at $z > 2.74$ hinder our ability to measure τ_{HeII} for individual systems with the high-resolution G130M. Many of the η -fluctuations appear at $z < 2.7$, observed with the lower-resolution G140L.

These small-scale η -variations have been the topic of numerous theoretical papers (Zuo 1992; Fardal & Shull 1993; Fardal et al. 1998; Bolton et al. 2005, 2006). The key focus of these papers is on fluctuations in the small numbers of AGN within the characteristic attenuation length, corresponding to the “ $\tau = 1$ sphere” at 4 ryd photon energy. Because the He II opacity is so much larger than that of H I, one expects large variations in the He II ionizing flux, J_{HeII} , on comoving scales of 20–40 Mpc at $z \approx 2.4 - 2.9$ (Fardal et al. 1998; Furlanetto 2009; Dixon & Furlanetto 2009). A second important effect is that the observed low-redshift AGN exhibit wide variations in their EUV spectral indices (Telfer et al. 2002; Scott et al. 2004), which produce strong source variations in the flux ratio $J_{\text{HeII}}/J_{\text{HI}}$. Finally, radiative transfer of the metagalactic ionizing radiation reprocesses the ionizing spectra, producing further variations (Fardal et al. 1998). What is now firmly established by the new COS data are the variations in η on ~ 10 Mpc comoving radial distance scales ($\Delta z \approx 0.01$).

3.6. Proximity Effect and Quasar Strömgren Spheres

It is surprising to note the sharpness of the He II edge at 1186.26 Å and the lack of any proximity effect near the QSO. If ionizing radiation were escaping from the AGN, the surrounding IGM should be ionized within 5–10 Mpc

of the QSO. The He II absorption extends $\Delta z \approx 0.019$ beyond the previous QSO redshift estimate, $z_{\text{em}} = 2.885$ (Reimers et al. 1997). As discussed in Section 3.1, this dilemma is easily resolved by moving the quasar redshift to $z = 2.904$, an offset (1460 km s^{-1} at $z = 2.9$) that corresponds to 19.5 Mpc comoving proper distance. However, the two proposed systemic redshifts, $z_{\text{QSO}} = 2.885$ and 2.904 , raise several questions. Does the QSO lie inside an H II and He III cavity produced by its photoionizing radiation? Or, is the QSO ionizing radiation absorbed by circumnuclear gas? Is there infalling gas near the AGN that produces associated absorption with $z_{\text{abs}} > z_{\text{em}}$? It is worth investigating these possibilities.

For H I (1 ryd) and He II (4-ryd) ionizing-photon luminosities, $S_0^{(\text{H})}$ and $S_0^{(\text{He})}$, what Strömgren radii will this bright QSO carve out? These distances are obviously limiting cases, in ionization equilibrium, whereas one expects the ionization zones around the QSO to involve time-dependent propagation of ionization fronts. Indeed, the lack of a proximity effect could arise from this source just starting to burn its way out of the galactic nucleus. Given the strength of the $z = 2.9$ absorber, we will assume higher gas densities associated with the QSO and scale to an overdensity ($\delta_H \approx 100$) at $z = 2.9$. The H and He densities are then: $n_{\text{H}} = (1.13 \times 10^{-3} \text{ cm}^{-3})(\delta_H/100)$, $n_e \approx 1.165 n_{\text{H}}$, and $n_{\text{He}} = (9.30 \times 10^{-5} \text{ cm}^{-3})(\delta_H/100)$. At $T = 10^{4.3}$ K, $\alpha_{\text{HeII}}^{(B)} = 9.1 \times 10^{-13} \text{ cm}^3 \text{ s}^{-1}$ and $\alpha_{\text{HI}}^{(B)} = 1.4 \times 10^{-13} \text{ cm}^3 \text{ s}^{-1}$. A typical (L^*) quasar produces a total of $\sim 10^{56}$ LyC photons s^{-1} , but this QSO is much brighter ($V = 16.1$). Extrapolation from 1200 Å down to the He II Lyman limit (889.5 Å at $z_{\text{QSO}} = 2.904$) shows that HE 2347-4342 has an observed specific flux, $F_\lambda \approx 6 \times 10^{-15} \text{ erg cm}^{-2} \text{ s}^{-1} \text{ Å}^{-1}$ or $F_\nu \approx 1.6 \times 10^{-27} \text{ erg cm}^{-2} \text{ s}^{-1} \text{ Hz}^{-1}$. From this flux and a luminosity distance, $d_L \approx 7.7 \times 10^{28} \text{ cm}$ at $z = 2.904$, we estimate an ionizing photon luminosity of $S_0^{(\text{He})} \approx \nu L_\nu/3 \approx 1.6 \times 10^{57}$ photons s^{-1} in the 4-ryd continuum. Scaling to $S_0^{(\text{He})} \approx 10^{57}$ photons s^{-1} , we estimate a He III Strömgren radius,

$$R_{\text{Str}}^{(\text{HeIII})} = \left[\frac{3S_0^{(\text{He})}}{4\pi n_e n_{\text{He}} \alpha_{\text{HeII}}^{(B)}} \right]^{1/3} \\ \approx (4 \text{ Mpc}) \left[\frac{S_0^{(\text{He})}}{10^{57} \text{ s}^{-1}} \right]^{1/3} (\delta_H/100)^{-2/3} T_{4.3}^{0.255}.$$

A similar calculation, using the observed flux, $F_\lambda \approx 1.2 \times 10^{-15} \text{ erg cm}^{-2} \text{ s}^{-1} \text{ Å}^{-1}$, at the redshifted (3561 Å) H I edge, gives $S_0^{(\text{H})} \approx \nu L_\nu/3 \approx 5 \times 10^{57}$ photons s^{-1} and an H II Strömgren radius of

$$R_{\text{Str}}^{(\text{HII})} = \left[\frac{3S_0^{(\text{H})}}{4\pi n_e n_{\text{H}} \alpha_{\text{HI}}^{(B)}} \right]^{1/3} \\ \approx (6 \text{ Mpc}) \left[\frac{S_0^{(\text{H})}}{5 \times 10^{57} \text{ s}^{-1}} \right]^{1/3} (\delta_H/100)^{-2/3} T_{4.3}^{0.286}.$$

We note that the ratio of the extrapolated fluxes at the respective ionization limits is fairly small. In the QSO

rest-frame, $F(912 \text{ \AA})/F(228 \text{ \AA}) \approx 5$, indicating a fairly hard (flat) power-law spectrum $F_\nu \propto \nu^{-1.2}$. These estimated Strömgren radii are a substantial fraction of the proper distance of 19.5 Mpc between the two proposed QSO redshifts, $z = 2.904$ and $z = 2.885$. Even though the local ionization zone may not extend as far as these equilibrium Strömgren radii, the expected proximity effect is minimally visible, except for a narrow feature with $\sim 60\%$ flux transmission at $z = 2.9055$, just below the He II edge (Figure 4). We conclude that ionizing radiation from this QSO is strongly absorbed in the proximity of the nucleus, possibly by circumnuclear gas or by the strong absorber at $z \approx 2.9$. The photoionization cross sections for H I and He II above threshold are approximately $\sigma_{\text{HI}} = (6.30 \times 10^{-18} \text{ cm}^2)(E/13.6 \text{ eV})^{-3}$ and $\sigma_{\text{HeII}} = (1.58 \times 10^{-18} \text{ cm}^2)(E/54.4 \text{ eV})^{-3}$. Thus, to absorb a substantial amount of the ionizing continua requires column densities

$$\begin{aligned} N_{\text{HI}} &= (1.59 \times 10^{17} \text{ cm}^{-2}) [E/13.6 \text{ eV}]^3 \tau(E) \\ N_{\text{HeII}} &= (6.35 \times 10^{17} \text{ cm}^{-2}) [E/54.4 \text{ eV}]^3 \tau(E) \end{aligned} \quad (9)$$

for continuum optical depth τ at photon energy E .

For this very bright QSO, the absence of a He II proximity effect indicates a significant attenuation of the 4 ryd continuum, with optical depth $\tau > 3$ at mean photon energies 1.5 times the 54.4 eV threshold, or $N_{\text{HeII}} > 6 \times 10^{18} \text{ cm}^{-2}$. What are the observational consequences of such large column densities of ionized gas? It has been suggested (Reimers et al. 1997) that O III resonance lines at 303.415 Å and 305.596 Å might be detectable, but we find no obvious candidates. It would be useful to search for signs of splittings of these lines, which are separated by $2.182 \text{ \AA}(1+z) \approx 8.5 \text{ \AA}$ at $z \approx 2.9$. Some of the associated absorbers have H I anomalously stronger than He II, suggesting that the gas is close to the QSO with helium mostly fully ionized (He III). More clues may come from the strong He II absorbers at $z = 2.900 - 2.904$ (1184.7–1186.2 Å) which would be closest to the QSO if $z_{\text{QSO}} = 2.904$. This system has high optical depth in both He II and H I (see Figure 4). Very strong metal-line absorption is seen in O VI with weaker absorption in C IV, C III, and N V (Reimers et al. 1997; Fechner et al. 2004). By fitting higher Lyman-series absorbers, Fechner et al. (2004) found $\log N_{\text{HI}} = 16.02 \pm 0.03$, while the metal-line absorbers gave $\log N_{\text{CIV}} = 13.66 \pm 0.03$, $\log N_{\text{NV}} = 13.42 \pm 0.04$, and $\log N_{\text{OVI}} \gtrsim 14.62$. They proposed that this absorber is exposed to the strongest and hardest radiation from the QSO, and therefore may shield the other associated absorbers. However, their photoionization models gave $\log N_{\text{HeII}} \approx 16.3$, which is 100 times too small to provide the necessary absorption (eq. [9]). The H I column is 10 times too small to shield the 1 ryd continuum.

Fox, Bergeron, & Petitjean (2008) obtained newer (high S/N) spectra on these metal-line absorbers at $z = 2.8916$, 2.8972 , and 2.9041 . They found somewhat higher column densities of C IV and N V and a slightly higher column density, $\log N_{\text{HI}} = 16.29 \pm 0.05$ in the $z = 2.9041$ absorber. This column is still insufficient to shield the QSO's ionizing continuum. We conclude that no satisfactory explanation exists for the absence of a proximity effect around this very luminous QSO, other

than the possibility that it has only recently turned on (within the last Myr).

4. CONCLUSIONS AND IMPLICATIONS

The high throughput and low background of the Cosmic Origins Spectrograph allow us to probe the He II reionization epoch toward HE 2347–4342 at redshifts $z = 2.4$ – 2.9 . Because of photoionization and recombination rates, He II is a far more abundant species than H I, with typical ratios $\eta = n_{\text{HeII}}/n_{\text{HI}}$ varying from 10–200 in the filaments of the Ly α forest. With COS, we find that reionization of He II to He III is patchy at $z = 2.7$ – 2.9 , with 5–10 Å troughs of high optical depth ($\tau_{\text{HeII}} > 5$) punctuated by narrow windows of flux transmission. Previous studies of this QSO sight line (Kriss et al. 2001; Shull et al. 2004; Zheng et al. 2004) found a gradual decrease in He II optical depth at $z < 2.7$, suggesting a He II reionization epoch $z_r = 2.8 \pm 0.2$. With our new COS data, we find a more complicated picture, in which He II is slowly reionized at $z \leq 2.7$.

We now summarize the new observational results and astrophysical issues:

1. We have found clear evidence that the epoch of He II reionization is delayed below $z = 3$, as we see patchy ionization down to $z \approx 2.7$. For this bright AGN, high-S/N, low-background observations from COS allow us to measure He II absorption, the UV continuum of the QSO, and troughs of high- τ_{HeII} . The high spectral resolution of the G130M grating probes absorption fluctuations and the He II ionization edge, and the G140L grating allows us to study He II reionization down to $z \approx 2.4$.
2. Comparison of COS/G130M and G140L data with previous *HST* and *FUSE* data confirms the far-FUV continuum, absorption troughs, transmission windows, and He II optical-depth below the He II edge at 1186.26 Å. The COS/G140L fluxes agree fairly well with *FUSE* data at $z > 2.7$ (Shull et al. 2004), but below 1130 Å ($z < 2.7$) considerable differences appear. The COS fluxes are lower than those of *FUSE* inferred by Zheng et al. (2004), and our derived He II optical depths are therefore somewhat higher at $2.4 < z < 2.7$. The broad-band optical depths (averaged over $\Delta z = 0.1$) only drop below $\langle \tau_{\text{HeII}} \rangle \leq 1$ at $z < 2.4$.
3. We observe optical-depth variations in He II and H I that imply fluctuations in the He II/H I abundance ratio on scales $\Delta z \approx 0.003 - 0.01$, corresponding to 4–10 Mpc in comoving distance. Such variations likely arise from AGN source variations (1–4 ryd spectral indices) and IGM radiative transfer effects. The number of low- η systems (mostly low τ_{HeII} and high τ_{HI}) seen with COS is lower than claimed in *FUSE* observations.
4. We see intervals of patchy He II flux-transmission, as well as three long (5–10 Å) intervals of strong He II absorption (25–60 Mpc proper distance) between $z = 2.751 - 2.807$, $z = 2.823 - 2.860$, and $z = 2.868 - 2.892$. These troughs probably arise from dense filaments in the baryon distribution and

the scarcity of strong photoionizing sources (AGN) within 30–50 Mpc.

5. At $z = 2.7\text{--}2.9$, probes of He II fraction, $x_{\text{HeII}} \geq (10^{-2})(0.1/\delta_{\text{He}})(\tau_{\text{HeII}}/5)$ are now possible at optical depths $\tau_{\text{HeII}} \geq 5$. The He II absorption is 50–100 times more sensitive to trace abundances than H I at $z = 6$, where a neutral fraction $x_{\text{HI}} = 10^{-4}$ saturates the Ly α Gunn-Peterson absorption.

What future work is needed to better understand the He II reionization? First, we need to assess whether the HE 2347–4342 sight line is typical. The COS-GTO team will be observing two more He II AGN targets, HS1700+6416 and Q0302-003, which may clarify whether the patchy reionization at $z < 2.8$ is common to most sight lines. Second, along the current sight line, we have identified many regions of partial flux transmission and three long troughs of He II absorption, where surveys of galaxies and AGN will help clarify the sources of ionization. Third, infrared spectra of the [O III] $\lambda 5007$, 4959 narrow emission lines (at 1.955 μm and 1.936 μm) could confirm the QSO systemic redshift. Pinning down z_{QSO} is crucial for understanding the nature of the ionization state of the gas near the QSO, which shows no evidence of a proximity effect. On the theoretical front, cosmological simulations with time-dependent H and He chemistry and I-front radiative transfer should elucidate the structure topology of the filaments and voids that we observe in the He II Ly α -forest and He II troughs.

Serious studies of He II reionization have been hindered by the lack of many AGN targets sufficiently bright to obtain far-UV spectra. The spectrographs on *FUSE* and *HST* have made good progress on three AGN sight lines, but newly discovered He II GP targets (Syphers et al. 2009a,b) are considerably fainter than HE 2347–4342 or HS1700+6416. New observations of these fainter targets will probably measure only broad-band He II optical depths, for which the high-resolution COS spectra may provide guidance in interpretation. The long-term study of the He II reionization process, from $z = 2.3\text{--}3.3$, must await the construction of a future large-aperture, far-UV telescope in space (Shull et al. 1999; Postman et al. 2009). It would be especially useful if this mission had high sensitivity and moderate spectral resolution ($R \gtrsim 20,000$) extending from 1130 Å down to the 912 Å hydrogen Lyman Limit. This would enable the study of patchy He II reionization in He II $\lambda 304$ down to redshifts $z \gtrsim 2$.

Telescope Science Institute. STScI is operated by the Association of Universities for Research in Astronomy, Inc. under NASA contract NAS5-26555. Our work was also supported by NASA grants NNX08AC146 and NAS5-98043 and the Astrophysical Theory Program (NNX07-AG77G from NASA and AST07-07474 from NSF) at the University of Colorado at Boulder.

It is our pleasure to acknowledge the thousands of people who made HST Servicing Mission 4 a huge success. We thank Brian Keeney, Steve Penton, Stéphane Béland, and the rest of the COS/GTO team for their work on the calibration and verification of the early COS data, and Cristina Oliveira for her helpful input on G140L segment-B CALCOS processing. We thank Dieter Reimers for discussions regarding the QSO systemic redshift and for providing VLT data on the H I Ly α forest. Mark Giroux, Blair Savage, David Syphers, and the referee provided numerous comments that improved the arguments made in this paper. This work is based on observations made with the NASA/ESA *Hubble Space Telescope*, obtained from the data archive at the Space

REFERENCES

- Barkana, R., & Loeb, A. 2001, *ARA&A*, 39, 19
- Bernardi, M., et al. 2003, *AJ*, 125, 32
- Bolton, J. S., & Haehnelt, M. G. 2007, *MNRAS*, 382, 325
- Bolton, J. S., Haehnelt, M. G., Viel, M., & Springel, M. 2005, *MNRAS*, 357, 1178
- Bolton, J. S., Haehnelt, M. G., Viel, M., & Carswell, R. F. 2006, *MNRAS*, 366, 1378
- Bolton, J. S., Oh, S. P., & Furlanetto, S. R. 2009, *MNRAS*, 395, 736
- Cen, R. 2003, *ApJ*, 591, L5
- Corbin, M. 1990, *ApJ*, 357, 346
- Dall’Aglio, A., Wisotzki, L., & Worseck, G. 2008a, *A&A*, 480, 359
- Dall’Aglio, A., Wisotzki, L., & Worseck, G. 2008b, *A&A*, 491, 465
- Danforth, C. W., & Shull, J. M. 2008, *ApJ*, 679, 194
- Danforth, C. W., Keeney, B. A., Stocke, J. T., Shull, J. M., & Yao, Y. 2010, *ApJ*, in press
- Davidson, A. F., Kriss, G. A., & Zheng, W. 1996, *Nature*, 380, 47
- Diplas, A., & Savage, B. D. 1994, *ApJ*, 427, 274
- Dixon, K. L., & Furlanetto, S. 2009, *ApJ*, 706, 970
- Espey, B. R., Carswell, R. F., Bailey, J. A., Smith, M. G., & Ward, M. J. 1989, *ApJ*, 342, 666
- Fan, X., et al. 2002, *AJ*, 123, 1247
- Fan, X., Carilli, C. L., & Keating, B. 2006, *ARA&A*, 44, 415
- Fardal, M., & Shull, J. M. 1993, *ApJ*, 415, 524
- Fardal, M., Giroux, M. L., & Shull, J. M. 1998, *AJ*, 115, 2206
- Faucher-Giguère, C.-A., Prochaska, J., Lidz, A., Hernquist, L., & Zaldarriaga, M. 2008, *ApJ*, 831
- Fechner, C., Baade, R., & Reimers, D. 2004, *A&A*, 418, 857
- Fechner, C., et al. 2006, *A&A*, 455, 91
- Fitzpatrick, E., & Massa, D. 1999, *PASP*, 111, 63
- Fox, A., Bergeron, J., & Petitjean, P. 2008, *MNRAS*, 388, 1557
- France, K., et al. 2010, *ApJ*, 715, 596
- Furlanetto, S. 2009a, *ApJ*, 700, 1666
- Furlanetto, S. 2009b, *ApJ*, 703, 702
- Furlanetto, S., & Dixon, K. L. 2010, *ApJ*, 714, 355
- Furlanetto, S., et al. 2009, *Astro2010: Astronomy and Astrophysics Decadal Survey Science White Papers*, No. 83 (arXiv:0902.3011)
- Gnedin, N. Yu., 2004, *ApJ*, 610, 9
- Green, J., et al. 2010, *ApJ*, in preparation
- Gunn, J. E., & Peterson, B. A. 1965, *ApJ*, 142, 1633
- Haardt, F., & Madau, P. 1996, *ApJ*, 461, 20
- Heap, S. R., et al. 2000, *ApJ*, 534, 69
- Hogan, C. J., Anderson, S. F., & Rugers, M. H. 1997, *AJ*, 113, 1495
- Jakobsen, P., et al. 1994, *Nature*, 370, 35
- Kim, T.-S., Bolton, J. S., Viel, M., Haehnelt, M. G., & Carswell, R. F. 2005, *MNRAS*, 382, 1657
- Komatsu, E., et al. 2010, *ApJS*, in press
- Kriss, G. A., et al. 2001, *Science*, 293, 1112
- Lidz, A., et al. 2010, *ApJ*, 718, 199
- McCandliss, S., et al. 2010, *ApJ*, 709, L183
- McDonald, P., et al. 2005, *ApJ*, 635, 761
- McQuinn, M. 2009, *ApJ*, 704, 89
- McQuinn, M., Lidz, A., Zaldarriaga, M., Hernquist, L., Hopkins, P. F., Dutta, S., & Faucher-Giguère, C.-A. 2009, *ApJ*, 694, 842
- Meiksin, A. 2009, *Rev. Mod. Phys.* 2009, 81, 1405
- Miralda-Escudé, J., Cen, R., Ostriker, J. P., & Rauch, M. 1996, *ApJ*, 471, 582
- Morton, D. C. 2003, *ApJS*, 139, 205
- Osterman, S., et al. 2010, *ApJ*, in preparation
- Osterbrock, D. E., & Ferland, G. J. 2006, *Astrophysics of Gaseous Nebulae and Active Galactic Nuclei*, (Sausalito, University Science Books).
- Peimbert, M., Luridiana, V., & Peimbert, A. 2007, *ApJ*, 666, 636
- Postman, M., et al. 2009, arXiv:0904.0941, *Advanced Technology Large Aperture Space Telescope*
- Reimers, D., Köhler, S., Wisotzki, L., Groote, D., Rodríguez-Pascual, P., Wamsteker, W. 1997, *A&A*, 327, 890
- Ricotti, M., Gnedin, N., & Shull, J. M. 2000, *ApJ*, 534, 41
- Ricotti, M., Gnedin, N., & Shull, J. M. 2002, *ApJ*, 575, 49
- Scannapieco, E., et al. 2006, *MNRAS*, 365, 615
- Schaye, J., et al. 2000, *MNRAS*, 318, 817
- Scott, J. E., et al. 2004, *ApJ*, 615, 135
- Shull, J. M., et al. 1999, arXiv:astro-ph/9907101, *The Emergence of the Modern Universe: Tracing the Cosmic Web*
- Shull, J. M., & Van Steenberg, M. E. 1985, *ApJ*, 294, 599
- Shull, J. M., & Venkatesan, A. 2008, *ApJ*, 685, 1
- Shull, J. M., Tumlinson, J., Giroux, M. L., Kriss, G. A., & Reimers, D. 2004, *ApJ*, 600, 570
- Smette, A., et al. 2002, *ApJ*, 564, 542
- Smith, B., Hallman, E., Shull, J. M., & O’Shea, B. 2010, *ApJ*, in preparation
- Sunyaev, R. 1977, *Akademia Nauk USSR, Astr. J. Letters*, 3, 491
- Syphers, D., et al. 2009a, *ApJ*, 690, 1181
- Syphers, D., et al. 2009a, *ApJS*, 185, 20
- Tegmark, M., Silk, J., Rees, M. J., Blanchard, A., Abel, T., & Palla, F. 1997, *ApJ*, 474, 1
- Telfer, R., Zheng, W., Kriss, G. A., & Davidson, A. F. 2002, *ApJ*, 656, 773
- Theuns, T., Bernardi, M., Frieman, Hewitt, P., Schaye, J., Sheth, R., & Subbarao, M. 2002, *ApJ*, 574, L111
- Trac, H., & Cen, R. 2007, *ApJ*, 671, 1
- Trenti, M., & Shull, J. M. 2010, *ApJ*, 712, 435
- Venkatesan, A., Tumlinson, J., & Shull, J. M. 2003, *ApJ*, 584, 621
- Weymann, R. J., Carswell, R. F., & Smith, M. G. 1981, *ARA&A*, 19, 41
- Worseck, G., Fechner, C., Wisotzki, L., & Dall’Aglio, A. 2007, *A&A*, 473, 805
- Zheng, W., et al. 2004, *ApJ*, 605, 631
- Zuo, L. 1992, *MNRAS*, 258, 36